



STRUCTURAL REPAIR OF HEAVILY DAMAGED REINFORCED CONCRETE  
COLUMNS: EXPERIMENTAL AND NUMERICAL STUDY

ÖZGÜR YURDAKUL

A THESIS SUBMITTED FOR  
THE DEGREE OF ASSOCIATE PROFESSOR

2023

# ABSTRACT

## HABILITATION THESIS

### STRUCTURAL REPAIR OF HEAVILY DAMAGED REINFORCED CONCRETE COLUMNS: EXPERIMENTAL AND NUMERICAL STUDY

**Ing. Özgür YURDAKUL, Ph.D.**

**2023, 86 Pages**

The response of substandard reinforced concrete (RC) columns and the structural repair of the pre-damaged columns by carbon-fiber-reinforced polymer sheets (CFRPs) were investigated by experimental and advanced numerical modeling methods. The specimens with non-conforming longitudinal and transverse reinforcement configurations were constructed from low-strength concrete and plain round bars. The investigated test parameters were the lap-splice, hook detail in the longitudinal reinforcement, and axial load ratio. First, the RC columns were tested up to failure under cyclic loading. Owing to the plain round bar and non-conforming details, the significant slip of the reinforcement governed the flexural response, which later developed axial damage (i.e., concrete crushing with reinforcement buckling). The severe cracks and concrete crushing were then successfully repaired by the externally bonded CFRP sheets. The former load-carrying capacities of the repaired RC columns were recovered, and the damage formation in the concrete and reinforcement was transferred to CFRP sheets. The final failure mode was characterized by local deformations in the CFRP with insignificant damage in the concrete and reinforcement bars. In addition, the nonlinear response of the as-built specimens was adequately reproduced in the finite element environment. The crack patterns and capacities of the numerical solutions matched well with the experimentally observed responses.

**Keywords:** Substandard; Low-strength concrete; Plain round bar; Column; CFRP; Repair

# ACKNOWLEDGMENTS

I am deeply grateful to my colleagues Ladislav ŘOUTIL, Bohumil CULEK, Petr VNENK, Vačlav ŠTECH, and Filip KLEJCH for their guidance, invaluable suggestions, technical expertise and help.

I would like to express my endless gratitude to Özgür AVŞAR (Eskişehir Technical University, Turkey) and Ciro DEL VECCHIO (University of Sannio, Italy) for their time and offering helpful comments.

This study has been accomplished with the support of the Educational and Research Centre in Transport, Transport Faculty, University of Pardubice. The support of MAPEI Company for providing the CFRP material and CEMEX for providing the concrete is gratefully acknowledged.

Finally, I wish to dedicate this thesis to my parents Gonca and Özkan YURDAKUL. This study would be nothing without their unconditional support and enduring love.

# TABLE OF CONTENTS

	<u>Page</u>
<b>ABSTRACT</b> .....	<b>ii</b>
<b>ACKNOWLEDGMENTS</b> .....	<b>iii</b>
<b>TABLE OF CONTENTS</b> .....	<b>iv</b>
<b>LIST OF FIGURES</b> .....	<b>vii</b>
<b>LIST OF TABLES</b> .....	<b>x</b>
<b>NOMENCLATURE</b> .....	<b>xi</b>
<b>1 INTRODUCTION</b> .....	<b>14</b>
1.1 Motivation.....	14
1.2 RC Profile: Reasons for Deficiencies .....	16
1.2.1 Material Properties.....	16
1.2.1.1 Low-Strength Concrete.....	16
1.2.1.2 Plain Round Bar .....	18
1.2.2 Geometric Parameters.....	19
1.2.2.1 Story Height.....	19
1.2.2.2 Column Dimensions .....	19
1.2.2.3 Reinforcement Ratio.....	20
1.2.2.4 High Axial Load .....	20
1.2.3 Detailing and Construction Practices.....	20
1.2.3.1 Insufficient Confinement.....	20
1.2.3.2 Specific Details of Reinforcement Elements.....	22
1.2.3.3 Insufficient Overlap of Reinforcement.....	24
1.2.3.4 Concrete Cover .....	24
1.2.4 Design Approach .....	25
1.2.4.1 Soft Story.....	25
1.2.4.2 Frame Discontinuity .....	26
1.3 RC Column Damage .....	26
1.3.1 Column Axial Failure .....	27

1.3.2	Strong Beam-Weak Column .....	27
1.3.3	Lap Splice (Bond-Slip) Failure .....	28
1.3.4	Column Shear Damage .....	29
1.3.5	Short Column .....	30
1.3.6	Captive Column .....	31
1.3.7	Accidental Captive Column .....	32
1.4	Repairability of RC Columns .....	34
1.5	Research Objective and Scope .....	38
1.6	Manuscript Organization .....	38
<b>2</b>	<b>EXPERIMENTAL PROGRAM .....</b>	<b>40</b>
2.1	Specimen Design .....	40
2.2	Test Setup, Procedure, and Instrumentation .....	42
2.3	Repair Design .....	44
2.3.1	Flexural Strengthening .....	44
2.3.2	Shear Strengthening .....	45
2.3.3	Ductility Enhancement .....	46
2.3.4	Anchor Design .....	47
2.4	Structural Repair .....	47
<b>3</b>	<b>NUMERICAL STUDY .....</b>	<b>50</b>
3.1	Numerical Model Description .....	50
3.2	Material Constitutive Laws .....	51
3.2.1	Concrete .....	51
3.2.2	Reinforcing Steel .....	53
3.2.3	Bond-Slip Model .....	54
3.2.4	Cold Joint .....	56
<b>4</b>	<b>ANALYSIS OF RESULTS .....</b>	<b>58</b>
4.1	Hysteric Response .....	58
4.1.1	As-Built Specimens .....	58
4.1.2	Repaired Specimens .....	64
4.2	Engineering Demand Parameters .....	68

4.2.1	Strength .....	68
4.2.2	Secant Stiffness and Displacement Ductility.....	70
4.2.3	Stiffness Degradation.....	71
4.2.4	Dissipated Energy .....	72
4.2.5	Experimental Moment-Curvature Response .....	73
4.3	Empirical Models .....	75
4.3.1	Damage Index .....	75
4.3.2	Drift at Axial Failure .....	76
4.3.3	Backbone Model and Performance Levels .....	77
<b>5</b>	<b>CONCLUSION .....</b>	<b>79</b>
5.1	Summary .....	79
5.2	Future Work .....	80
	<b>REFERENCES.....</b>	<b>81</b>

# LIST OF FIGURES

Fig. 1.1. Damage distribution among the investigated 61152 buildings by February 08, 2020 (Yurdakul et al. 2021).....	16
Fig. 1.2. (a) Aggregate size in slightly/moderately damaged buildings (b) organic material in concrete (Yurdakul et al. 2021). ....	17
Fig. 1.3. Concrete strength distribution in İstanbul and surrounding cities (Bal et al. 2008) and comparison with the minimum code requirements.....	18
Fig. 1.4. RC member with plain round bar (Yurdakul et al. 2021). ....	19
Fig. 1.5. Distribution of regular-story height for all RC buildings (Bal et al. 2008).....	19
Fig. 1.6. Axial load distribution.....	20
Fig. 1.7. Insufficient confinement-data from (a) Yurdakul <i>et al.</i> (2021) (b) Ricci <i>et al.</i> (2011). ....	22
Fig. 1.8. Hook details of seismic hoops in column (a) plain round bars (b) deformed bars (Yurdakul et al. 2021).....	23
Fig. 1.9. Unengaged longitudinal bar (Yurdakul et al. 2021).....	23
Fig. 1.10. Reinforcing detail without crossties (Yurdakul et al. 2021). ....	24
Fig. 1.11. Reported lap splice failure by Naseer <i>et al.</i> (2010).....	24
Fig. 1.12. Corroded reinforcement (Yurdakul et al. 2021).....	25
Fig. 1.13. Soft story induced damage in Maraş Earthquake 2023 (Photo Credit: Yunus Demirtaş).....	25
Fig. 1.14. Frame discontinuity (Yurdakul et al. 2021). ....	26
Fig. 1.15. Column axial failure (a) Van 2011 earthquake, Turkey (Öztürk 2015) (b) Kütahya-Simav 2011 earthquake (Yılmaz and Avşar 2013) (c) L’Aquila 2009 earthquake, Italy (Ricci et al. 2011) (d) İzmir Seferihisar 2020 earthquake, Turkey (Photo Credit: Özgür Avşar).....	27
Fig. 1.16. Strong beam-weak column failure (a) Van 2011 earthquake, Turkey (Öztürk 2015) (b) Kashmir 2005 earthquake, Pakistan (Naseer et al. 2010). ....	28
Fig. 1.17. Reported lap splice failure (a) Çagatay (2005) (b) Elwood (2006).....	28
Fig. 1.18. Column shear damage (Yurdakul et al. 2021).....	29

Fig. 1.19. Short column due to structural element (a) Elazığ 2020 earthquake, Turkey (Yurdakul et al. 2021) (b) Van 2011 earthquake, Turkey (Öztürk 2015) (c) L'Aquila 2009 earthquake, Italy (Ricci et al. 2011). .....	30
Fig. 1.20. Captive column due to ribbon window (Yurdakul et al. 2021). .....	31
Fig. 1.21. Accidental captive column (a) Elazığ 2020 earthquake, Turkey (Yurdakul et al. 2021) (b) İzmir Seferihisar 2020 earthquake, Turkey (Photo Credit: Özgür Avşar). .....	33
Fig. 2.1. Reinforcement scheme (a) continuous without lap-splice length (b) confirming configuration with hooks (c) non-conforming configuration without hooks.....	42
Fig. 2.2. Test setup. ....	43
Fig. 2.3. Displacement history. ....	43
Fig. 2.4. Instrumentation on specimens. ....	44
Fig. 2.5. Illustration of the dimensional variables used in shear-strengthening calculations for repair, retrofit or strengthening using FRP laminates (figure from ACI 440.2R-17 (2017)). .	46
Fig. 2.6. Repair of RC column by CFRP. ....	48
Fig. 3.1. (a) Concrete behavior under compression, (b) Compression softening, (c) Strength reduction in the cracked concrete (ATENA Program Documentation, Part 1 2014). ....	52
Fig. 3.2. (a) Tension softening and (b) Shear retention factor (ATENA Program Documentation, Part 1 2014). ....	52
Fig. 3.3. Cyclic bond-slip model for specimens with confinement (Yurdakul et al. (2022)). .	55
Fig. 4.1. Hysteric response of as-built specimens (a) E1-T-H (b) E1-C-H (c) E1-NC-H (d) E1-T-L (e) E1-C-L (f) E1-NC-L.....	62
Fig. 4.2 (cont.). Damage evaluation in as-built specimens (a) E1-T-H (b) E1-C-H (c) E1-NC-H (d) E1-T-L (e) E1-C-L (f) E1-NC-L. ....	64
Fig. 4.3. Hysteric response of repaired specimens (a) E1-T-H-R (b) E1-C-H-R (c) E1-NC-H-R (d) E1-T-L-R (e) E1-C-L-R. (f) E1-NC-L-R. ....	66
Fig. 4.4 (cont.). Damage evaluation in repaired specimens (a) E1-T-H-R (b) E1-C-H-R (c) E1-NC-H-R (d) E1-T-L-R (e) E1-C-L-R. (f) E1-NC-L-R. ....	68
Fig. 4.5. Comparison of hysteric responses specimen with (a) high axial load and no lap-splice (b) high axial load and conforming hook (c) high axial load and non-conforming hook (d) low axial load and no lap-splice (e) low axial load and conforming hook (f) low axial load and non-conforming hook. ....	69

Fig. 4.6. Backbone curves of hysteric response (a) as-built specimens (b) repaired specimens. .....	70
Fig. 4.7. Stiffness degradation (a) as-built specimens (b) repaired specimens. ....	72
Fig. 4.8. Dissipated energy (a) as-built specimens (b) repaired specimens. ....	72
Fig. 4.9. Computation of curvature. ....	73
Fig. 4.10. Experimental moment-curvature relationship of reference specimens (a) E1-T-H (b) E1-C-H (c) E1-NC-H (d) E1-T-L (e) E1-C-L (f) E1-NC-L. ....	74
Fig. 4.11. Experimental moment-curvature relationship of repaired specimens (a) E1-T-H-R (b) E1-C-H-R (c) E1-NC-H-R (d) E1-T-L-R (e) E1-C-L-R (f) E1-NC-L-R. ....	75
Fig. 4.12. Damage index (a) as-built specimens (b) repaired specimens. ....	76
Fig. 4.13. IDR at axial failure (a) as-built specimens with high axial load (b) as-built specimens with low axial load. ....	77
Fig. 4.14. Comparison of ASCE SEI 41 (2017) backbone models with hysteric responses (a) E1-T-H (b) E1-C-H (c) E1-NC-H (d) E1-T-L (e) E1-C-L (f) E1-NC-L. ....	78

# LIST OF TABLES

Table 1.1. Summary of damage levels and corresponding repair actions.....	36
Table 2.1. Target geometrical and material parameters retrieved from available literature. ....	41
Table 2.2. Details of tested specimens. ....	49
Table 3.1. Summary of adapted concrete material properties.....	53
Table 3.2. Summary of adapted reinforcing steel material properties. ....	54
Table 3.3. Summary of cold joint parameters. ....	57
Table 4.1. Summary of measured damage quantities. ....	62
Table 4.2. Summary of engineering demand parameters.....	71

# NOMENCLATURE

$A_c$	: Cross sectional area
$A_s$	: Area of longitudinal reinforcement
$A_{st}$	: Area of shear reinforcement
$A_{sur}$	: Surface area
$c$	: Strength reduction factor in the cracked concrete
$c_s$	: Distance from extreme compression fiber to neutral axis
$c_o$	: Cohesion
$C_v$	: Coefficient of variation
$d_b$	: Bar diameter
$d_{ba}$	: Diameter of fiber anchor
$d_c$	: Depth of column core from center to center of ties
$d_f$	: Effective depth of FRP
$d_{f,s}$	: Height of FRP from end of sheet to center of longitudinal reinforcement
$E_{c,res}$	: Elastic modulus of epoxy resin in compression
$E_{t,res}$	: Elastic modulus of epoxy resin in tension
$E_c$	: Elastic modulus of concrete
$E_d$	: Dissipated energy
$E_f$	: Elastic modulus of CFRP sheets
$E_s$	: Elastic modulus of reinforcing steel
$F$	: Force
$f_c$	: Compressive strength of concrete
$f_{b,res}$	: Bond strength; pull-out
$f_{c,res}$	: Compressive strength of epoxy resin
$f_{co}$	: Compressive strength at start of inelastic response
$f_{cr}$	: Reduced compressive strength in the cracked concrete
$f_{ct}$	: Tensile strength of concrete
$f_{ct,res}$	: Tensile strength of epoxy resin
$f_{ct,i}$	: Tensile strength of interface
$f_f$	: Tensile strength of CFRP sheets
$f_{fd}$	: Design axial stress in anchor
$f_{cts,res}$	: Shear strength of epoxy resin
$f_e$	: Lateral confinement pressure
$f_u$	: Ultimate strength of longitudinal reinforcing steel
$f_{ut}$	: Ultimate strength of shear reinforcement
$f_y$	: Yield strength of reinforcing steel
$f_{yt}$	: Yield strength of shear reinforcement
$F_t$	: Tensile force
$G$	: Reduced shear modulus

$G_c$	: Shear modulus of concrete
$G_f$	: Fracture energy of concrete
$G_{f,res}$	: Fracture energy of epoxy resin
$K$	: Secant Stiffness
$K_{nn}$	: Nominal stiffness of interface material
$K_{tt}$	: Tangential stiffness of interface material
$L$	: Column height
$L_b$	: Plastic hinge length
$l_{df}$	: Development length
$L_{ds}$	: Distance between measuring point of two sensors in horizontal direction
$L_{eff}$	: Effective height
$L_t$	: Finite element size
$L_{Lo}$	: Original length between vertical laser displacement sensors
$M$	: Moment
$N$	: Axial load
$n_f$	: Number of CFRP layer
$r_g(\varepsilon)$	: Shear retention factor
$t_f$	: Thickness of FRP sheet
$S_s$	: Stirrup spacing
$S_{c1}$	: Slip at ultimate bond stress
$S_{c2}$	: Slip at residual bond stress
$V_c$	: Column shear
$V_{frp,F}$	: Contribution of FRP to flexural strength
$V_{frp,required}$	: Required additional shear strength
$V_{frp,S}$	: Contribution of FRP to shear strength
$w$	: Deformation in fracture process zone
$w_1$	: Crack width when tensile stress reaches 20% of tensile strength
$w_c$	: Fictitious crack opening at complete stress release
$w_d$	: Plastic displacement at complete stress release
$w_f$	: Width of CFRP layer
$w_o$	: Displacement at ultimate concrete compressive strength
$\alpha$	: Angle
$\alpha_b$	: Shape factor in bond-slip model
$\beta_{c,b}$	: Confinement factor
$\Delta$	: Displacement
$\Delta_{y,frp}$	: Yield deflection in FRP strengthened member
$\Delta_{p,frp}$	: Plastic deflection in FRP strengthened member
$\Delta_u$	: Ultimate displacement taken at 20% strength loss
$\Delta_y$	: Displacement at effective yielding
$\Delta_{1.2}$	: Measured displacement change
$\delta$	: Drift

$\delta_u$	: Ultimate IDR taken at 20% strength loss
$\delta_y$	: IDR at effective yielding
$\varepsilon$	: Strain at any state
$\varepsilon_{bi}$	: initial strain of bonded substrate from elastic analysis
$\varepsilon_{co}$	: Strain corresponding to the ultimate strength of concrete
$\varepsilon_{cos}$	: Strain corresponding to the ultimate strength of epoxy resin
$\varepsilon_{cr}$	: Concrete cracking strain
$\varepsilon_{cu}$	: Ultimate compressive strain of concrete
$\varepsilon_{fd}$	: Debonding strain
$\varepsilon_{fe}$	: Effective strain of FRP
$\varepsilon_{fu}$	: Rupture strain of FRP
$\varepsilon_o$	: Strain corresponding to the ultimate strength of reinforcing bar
$\varepsilon_u$	: Ultimate strain of reinforcing steel
$\varepsilon_y$	: Yield strain of reinforcing steel
$\varepsilon_{1,2}$	: Computed strains
$\gamma$	: Shear strain
$\phi$	: Curvature
$\phi_s$	: Safety factor
$\phi_{y,frp}$	: Yield curvature of FRP strengthened section
$\phi_{u,frp}$	: Ultimate curvature of FRP strengthened section
$\mu$	: Mean value
$\mu_c$	: Coefficient of friction
$\mu_d$	: Displacement ductility
$\psi$	: Strength reduction factor
$\rho$	: Longitudinal reinforcement ratio
$\sigma$	: Stress
$\sigma_N$	: Axial load ratio
$\sigma_r$	: Standard deviation
$\tau$	: Shear stress
$\tau_b$	: Bond stress
$\tau_c$	: Bond stress in confined concrete
$\tau_r$	: Shear strength with dowel action
$\theta$	: Angle

### **Abbreviations**

CFRP	: Carbon fiber reinforced polymers
FE	: Finite element
FEM	: Finite element method
LVDT	: Linear variable displacement transducer
RC	: Reinforced concrete
IDR	: Inter-story drift ratio

# 1

## INTRODUCTION

---

The current study targets to evaluate the performance of heavily damaged reinforced concrete (RC) columns, which are repaired by Carbon Fiber Reinforced Polymers (CFRPs). This is intended to be achieved for all specimens through laboratory tests and experimentally validated numerical models. First, the experimental response of as-built RC columns is obtained through six full-scale tests. Then, the heavily damaged substandard RC columns are repaired by CFRPs and tested again. Finally, the whole procedure is also simulated in a finite element (FE) environment.

### 1.1 Motivation

According to the capacity design principles specified in most modern design codes, structural members should exhibit a ductile response. Several codes and guidelines describe the requirements to meet the ductile behavior and design principles (CEN 2004a; NZS 3101 2006; ACI 318 2019). However, a significant portion of RC buildings in the existing building inventory of developing countries has specific local deficiencies, which can cause premature failure of structural members (Tezcan et al. 1978; Norton et al. 1994; Ricci et al. 2011; Yılmaz and Avşar 2013; Angster et al. 2015; Kc et al. 2019; Yurdakul et al. 2021). Structural deficiencies mainly arising from poor material properties (e.g., use of low-strength concrete and plain round bars), improper detailing in RC components, and unaudited construction may result in devastating brittle failure. Severe damage at the RC member remarkably violates the integrity of the structural system. The obvious outcomes are poor energy dissipation and sudden

strength and stiffness degradation. As local damages can also actuate the global failure mechanism, investigating the behavior of substandard members is essential. Based on field observations and laboratory tests, capacity design principles have earmarked deficient RC members as critical components in the moment-resisting frames (Yurdakul et al. 2021). This poses a severe societal risk (Del Vecchio et al. 2020).

A structure during its economic lifetime may face a low probability event such as earthquakes or natural and man-made disasters. Note that the design codes allow a certain level of damage (ensuring life safety without total collapse), which can make the building unserviceable in such low probable events. Indeed, good performance of buildings was observed in the Canterbury earthquakes in 2010 and 2011, with fewer fatalities (185 deaths) (Parker and Steenkamp 2012). However, the rebuild costs of around NZ\$20 billion (US\$15 billion), excluding disruption costs, or 10% of GDP, are estimated. The insured losses of around NZ\$30 billion (US\$25 billion) are reported by the National reserve bank of New Zealand (Parker and Steenkamp 2012). Therefore, minimizing the rebuilding costs could be necessary to decrease the economic impacts of natural disasters.

The Disaster and Emergency Management Presidency of Türkiye estimated the economic loss of Van, Turkey Earthquake in 2011 around 2.9 billion dollars (AFAD 2012).

One of the deadliest earthquake hit L'Aquila, Italy in 2009 killed 309 people, injured 1600 people, and caused more than 65000 people homeless, with estimated direct economic loss of 540 million euro (US\$590 million) (Di Pietro and Mora 2015).

The preliminary damage observations conducted by the Ministry of Environment and Urbanisation (MoEU (2020)) report the damage level after an earthquake with a magnitude  $M_w$  of 6.8 hit Elazığ Province in Turkey on January 24<sup>th</sup>, 2020 (DEMP 2020). A total of 17021 buildings were reported as slightly damaged. Among 61152 inspected buildings, those with moderate and heavy damage were 1492 and 8396, respectively (Fig. 1.1). Besides, a total of 821 buildings were marked to be immediately demolished or totally collapsed (e.g., during the earthquake, 3 RC buildings totally collapsed). 33422 buildings were marked to be undamaged. The majority of these buildings (specifically moderate and severe damage ones) are demolished just after the earthquake event without considering any economic aspects.

The economic balance sheet of the Maraş-Türkiye Earthquake on February 6<sup>th</sup>, 2023 was calculated by factoring in the amount to be spent on reconstruction, reinforcement, and repair

of the destroyed and damaged homes and workplaces, debris removal and emergency rescue operations, income aid to be provided by the state to earthquake victims, and the state's income tax loss.

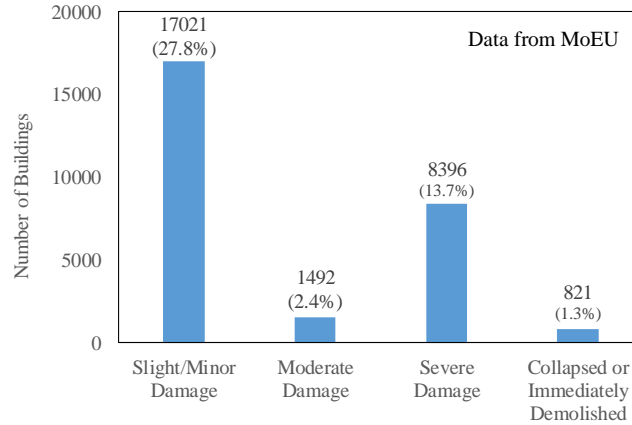


Fig. 1.1. Damage distribution among the investigated 61152 buildings by February 08, 2020 (Yurdakul et al. 2021).

The repair action should be taken for the structures, which are supposed to be serviceable after reaching the deformation limit of serviceability. According to FEMA P-58 (2018), the threshold for the economic feasibility of repair is specified when the ratio of repair cost-to replacement cost is about 50 %. Moderate to severe damage structures are often demolished even without reaching that economic limit (Yurdakul et al. 2021). Besides, additional adverse effects such as (i) mass demolition work (together with environmental aspects); (ii) insufficient housing in a short time; (iii) and intrusive construction work may lead to relatively high direct and indirect costs. These prove the significance of a reliable repair strategy for heavily damaged RC members. Particularly, developing an innovative repair solution becomes a key point. Since the RC column members are one of the weakest and most critical structural elements in a framed structure according to capacity design and hierarchy of strength, this study focuses on substandard RC columns.

## 1.2 RC Profile: Reasons for Deficiencies

### 1.2.1 Material Properties

#### 1.2.1.1 Low-Strength Concrete

The field observations have vitally earmarked the use of low-strength concrete as the main deficiency in moment-resisting frame structures in the Mediterranean area (Yılmaz and Avşar 2013). The main reasons behind this are high water-cement ratio, lack of proper curing,

improper aggregate size and type (Fig. 1.2a), and organic materials in the concrete (Fig. 1.2b) (Yurdakul et al. 2021).



(a)



(b)

Fig. 1.2. (a) Aggregate size in slightly/moderately damaged buildings (b) organic material in concrete (Yurdakul et al. 2021).

Bal *et al.* (2008) found the mean value of compressive strength as 16.73 MPa in existing RC Buildings in İstanbul, Turkey (Fig. 1.3). A more dramatic concrete compressive strength value (10.35 MPa) was reported in a collapsed building in Ceyhan, Turkey (Çağatay 2005). Mazılıgüney *et al.* (2008) analyzed the compressive strength of 4647 core specimens taken from 693 buildings in Istanbul, Turkey. The resulting mean value was 10.64 MPa, which also supports the other findings. After inspecting the RC buildings of Elazığ province in 2020 after the earthquake, the Turkish Ready Mixed Concrete Association (TRMCA 2020) reported the mean compressive strength between 6-12 MPa. Arslan and Korkmaz (2007) concluded that the average concrete compressive strength that was taken from damaged and undamaged buildings was as low as 1/3 of the design strengths. Del Vecchio *et al.* (2018) reported the average compressive strength of concrete as 11.92 MPa in a building demolished after the L'Aquila Earthquake, Italy. Masi and Vona (2009) worked on 824 concrete core samples in more than 200 RC buildings in Italy and found an average compressive strength of 12–16 MPa in 93 of

824 tests. In Japan, Shimizu *et al.* (2000) found the average compressive strength to be less than 13.50 MPa in some of the inspected buildings, which comprise 3.3% of the total. The frequency of buildings with an average compressive strength of 16.00 MPa is above 5%.

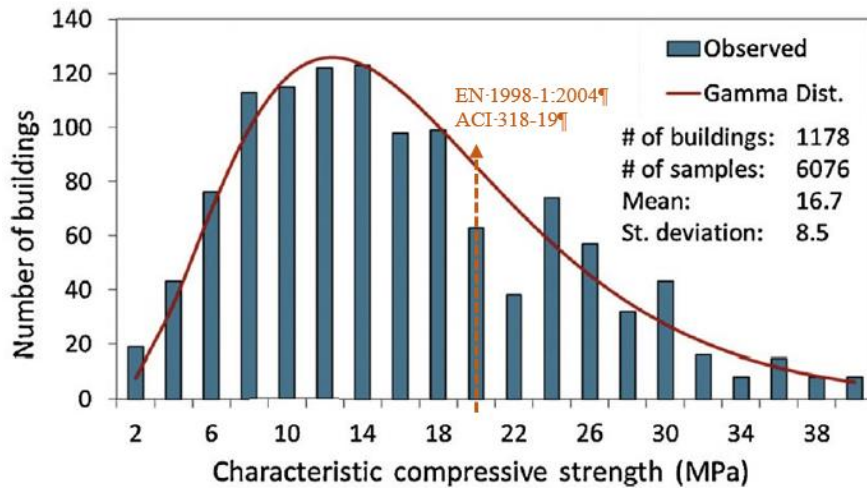


Fig. 1.3. Concrete strength distribution in İstanbul and surrounding cities (Bal et al. 2008) and comparison with the minimum code requirements.

American Concrete Institute (ACI) defines the minimum concrete compressive strength as 20 MPa (3000 psi) for special moment frames in ACI 318-19 (2019). The European standard (in the design of earthquake resistive structures EN 1998-1:2004 (CEN 2004b)) limits the minimum concrete compressive strength to 20 MPa for DCH (High Ductile Class) in primary seismic elements. However, all on-site compressive strength values comprising most of the structures are well below the values accepted universally as normal strength concrete (20 MPa in many standards). Overall, the compressive strength values lower than the 20 MPa is assumed to be poor-quality concrete.

### 1.2.1.2 Plain Round Bar

The use of plain round bars could exhibit a poor bond performance as the other types of failures are usually preceded by bond-slip failure (Fig. 1.4). Therefore, structures with plain round bars are usually considered to be substandard with respect to today's construction practices. In these structures, the required level of interaction between concrete and a reinforcing bar could not be ensured, which results in bond-slip failure together with anchorage pull-out failure (Bull et al. 2009). The cohesion between reinforcing steel and concrete can be easily influenced by other factors such as concrete mechanical properties, level of confinement, clear cover, casting position, and geometric details (i.e., bar size and spacing) (ACI 408R-03 2003; Murcia-Delso 2013). The increase in the slump due to a high water-cement ratio, which is quite common for low-strength concrete, adversely affects the bond response, as well.



Fig. 1.4. RC member with plain round bar (Yurdakul et al. 2021).

## 1.2.2 Geometric Parameters

### 1.2.2.1 Story Height

The mean value of the story height for 938 sample buildings in İstanbul and surrounding cities in Turkey is reported as 2.84 m with  $C_v$  of 8% (Bal et al. 2008). The data is visually depicted in Fig. 1.5. A similar value is also stated in other studies. Depending on the year and story height, the range of ground story level is reported as 2.87-3.36 m with  $C_v$  of 8% and 30% (Ozmen et al. 2015).

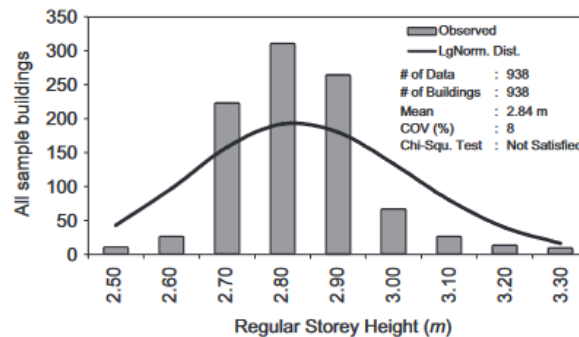


Fig. 1.5. Distribution of regular-story height for all RC buildings (Bal et al. 2008).

### 1.2.2.2 Column Dimensions

Data from existing building stock shows that the mean value of the column width varies between 255-334 mm with a relatively high scatter (Ozmen et al. 2015). Depending on the year and story height, the coefficient of variation  $C_v$  in column width varies around 8%-20% (Ozmen et al. 2015). The column depth also varies between 490-746 mm with the coefficient of variation  $C_v$  of 0.12-0.35. Bal *et al.* (Bal et al. 2008) reported the column depth in İstanbul and surrounding cities as 450 mm, 490 mm, 650 mm, and 700 mm for less or equal to 3-story, 4-story, 5-story, and 6- and more story frames, respectively.

### 1.2.2.3 Reinforcement Ratio

The longitudinal steel ratio of columns is reported between 0.96-1.14 % with  $C_v$  of 12% and 33% (Ozmen et al. 2015). Current and former standards also limit the minimum longitudinal steel ratio to 1% (TEC 1975; CEN 2004a). It seems that the minimum reinforcement is replaced in the existing buildings.

### 1.2.2.4 High Axial Load

The current study targets to evaluate the axial load ratio ( $\sigma_n=N/A_c f_c$ ) in substandard existing buildings, where  $N$  is axial load,  $A_c$  is the cross-sectional area, and  $f_c$  is concrete compressive strength. Based on the 284 observations in the buildings located in İstanbul, Turkey, the mean value  $\mu$  of axial load ratio  $\sigma_n$  is found as 0.32 (Fig. 1.6). The standard deviation  $\sigma_r$  is computed as 0.17. Weibull is the best-fit distribution for the provided data. The chi-square and Kolmogorov-Smirnov tests are satisfied at a 95% significance level. Note that EN1998-1:2004 (CEN 2004b) limits the axial load ratio to 0.55 for high ductility class buildings. However, many of the reported axial load ratios are higher than the limit (specifically, the ones beyond the prominent upper range).

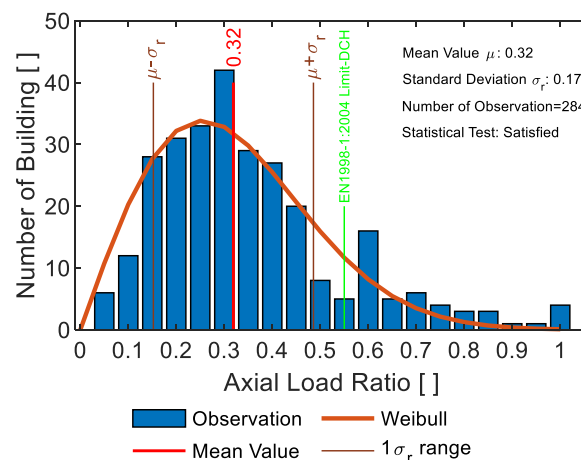


Fig. 1.6. Axial load distribution.

## 1.2.3 Detailing and Construction Practices

### 1.2.3.1 Insufficient Confinement

The failures related to insufficient confinement of RC members should attract attention since they remarkably compromise the structural redundancy. The special confinement zones arranged at the member ends should be provided in many standards (CEN 2004b; NZS 3101 2006; ACI 318 2019). According to EN1998-1:2004 (CEN 2004b), the confinement zone

length at column ends shall not be less than smaller of [1/6 of the clear height of the column (measured upward from floor level or downward from the bottom face of the deepest beam framing into the column), column largest section dimension, and 450 mm]. The horizontal confinement reinforcement in joints of primary seismic beams with columns should be not less than that specified limit in EN1998-1:2004 (CEN 2004b) as well.

The reconnaissance on the inspected RC members has shown no or low-level of confinement at member-ends. The spacing of the transverse reinforcement was measured around 25-30 cm in a non-uniform fashion in many of the inspected buildings, which is well above the accepted limits (Fig. 1.7a and b). The large spacing of transverse reinforcement has resulted in an increased unsupported length of longitudinal bars and hence less buckling resistance. Moreover, the inadequate number of stirrups with improper detailing reduced the beam-column joint shear capacity. As a result, shear cracks were observed in several inspected RC buildings. Devastating shear failure of the beam-column joints was reported in L'Aquila 2009 earthquake, Italy by Ricci *et al.* (2011). The main reason is the lack of shear reinforcement.



(a)



(b)

Fig. 1.7. Insufficient confinement-data from (a) Yurdakul *et al.* (2021) (b) Ricci *et al.* (2011).

### 1.2.3.2 Specific Details of Reinforcement Elements

Special seismic hoops and cross ties shall be provided for RC sections in all seismic zones. According to EN1998-1:2004 (CEN 2004b), the seismic hoops should have  $135^\circ$  hooks with  $10d_{bw}$  anchorage length at both ends, where  $d_{bw}$  is the stirrup diameter. However, those were not provided in the reported studies (Fig. 1.8a and b). The stirrups were bent improperly with  $90^\circ$  hooks, which is non-conforming even with the current and former standards.



Fig. 1.8. Hook details of seismic hoops in column (a) plain round bars (b) deformed bars (Yurdakul et al. 2021).

The stirrups should engage the longitudinal reinforcement from the outside (EN1998-1:2004 (CEN 2004b)). Both hooks of the stirrups shall be closed around the same longitudinal bar. On the other hand, as an example of poor workmanship in the reported column members, some of the column longitudinal bars were out of the confined region, which could possibly cause reinforcement buckling (Fig. 1.9).



Fig. 1.9. Unengaged longitudinal bar (Yurdakul et al. 2021).

Providing crossties with proper spacing links the column longitudinal bars at opposite sides, which increases the buckling resistance of the longitudinal bars, and thereby prevents the opening of the stirrups. This is one of the most critical detailing requirements for the transverse reinforcement in providing the integrity of the RC column sections. Without the presence of crossties, it is almost not possible to restrain the longitudinal bars with the flexural stiffness of perimeter hoops only. The arrangement of crossties arranged in the columns was also enforced in EN1998-1:2004 (CEN 2004b). On the other hand, the code requirements were not fulfilled in many of the reported buildings (Fig. 1.10).



Fig. 1.10. Reinforcing detail without cross-ties (Yurdakul et al. 2021).

### 1.2.3.3 Insufficient Overlap of Reinforcement

The assumption of the perfect bond between the concrete and reinforcement bar is one of the most fundamental assumptions. The use of plain round bars in many buildings constructed in the 70s cannot or can barely satisfy the required level of interaction. Besides, the necessary hook details (i.e.,  $180^\circ$ ) at the end of the members with the required overlapping distance shall be provided for plain round bars. On the other hand, non-seismically designed and detailed RC buildings lack such important criteria (Fig. 1.11).



Fig. 1.11. Reported lap splice failure by Naseer *et al.* (2010).

### 1.2.3.4 Concrete Cover

The bond mechanism is violated not only by detailing issues but also by corrosion. Insufficient concrete cover and harsh environmental conditions accelerated the corrosion mechanism, which actuates the corrosion-induced cracks in concrete. Those, as a side effect, result in the loss of interaction between concrete and reinforcing steel, and diameter decrement in the bar (Fig. 1.12).



Fig. 1.12. Corroded reinforcement (Yurdakul et al. 2021).

## 1.2.4 Design Approach

### 1.2.4.1 Soft Story

A very typical design practice in the conventional building stock of Mediterranean countries is to have commercial units on the ground floor with either larger openings in the infill walls or without any infill walls. Ground story height is usually higher than the normal stories used for residential purposes. The soft stories are usually designed as a shop, parking garage, or storage purposes. On the other hand, the stiffness provided by the infill walls reduces the deformation in the upper stories, while the elimination of infill walls causes more lateral deformation in the ground story. The increased column deformations localized at the ground level are not foreseen in the design stage if the effect of infill walls is not considered in the structural analysis. This may cause local damage or even total collapse of the structure due to the formation of the soft-story mechanism. Moreover, non-structural components at the ground story suffer from more damage due to larger inter-story drift demands (Fig. 1.13).



Fig. 1.13. Soft story induced damage in Maraş Earthquake 2023 (Photo Credit: Yunus Demirtaş)

#### 1.2.4.2 Frame Discontinuity

The frame irregularity is characterized by discontinuities in the vertical or horizontal directions, which adversely affects the performance of buildings. Several types of frame irregularities are found in some of the reported buildings, which were graded as moderately damaged buildings (Fig. 1.14). To transfer the inertial forces, mainly developed at the floor level from floors to the ground, the frame components should be continuously connected to each other from their geometric axis as much as possible. However, numerous frame discontinuity examples were reported (Yurdakul et al. 2021).



Fig. 1.14. Frame discontinuity (Yurdakul et al. 2021).

In addition to the above-mentioned deficiencies, large and heavy overhangs, and poor frame-infill interaction etc., are the main issues at the design and manufacturing levels of substandard RC structures (Arslan and Korkmaz 2007). The secondary effects of non-structural components on global behavior are also critical for these structures.

### 1.3 RC Column Damage

This study focuses on the substandard RC columns since they are one of the weakest and most critical structural elements according to capacity design and hierarchy of strength. Therefore, the most common RC column damages reported after field reconnaissance surveys are summarized in this section.

### 1.3.1 Column Axial Failure

The spacing of the transverse reinforcement is measured around 25-30 cm in a non-uniform fashion in many of the inspected buildings, which is well above the accepted limits (Fig. 1.7a and b). Under-designed columns lead the premature shear damage, which can be followed by axial failure of the column. Note that the large spacing of transverse reinforcement has resulted in an increased unsupported length of longitudinal bars, and hence less buckling resistance. Besides, the complete opening of hoops, together with the lack of cross ties, decrease the buckling resistance of the reinforcement. The use of low-strength concrete leads to the crushing of concrete. As a result, the axial-load-bearing capacity of the RC column is lost (Fig. 1.15a-d).

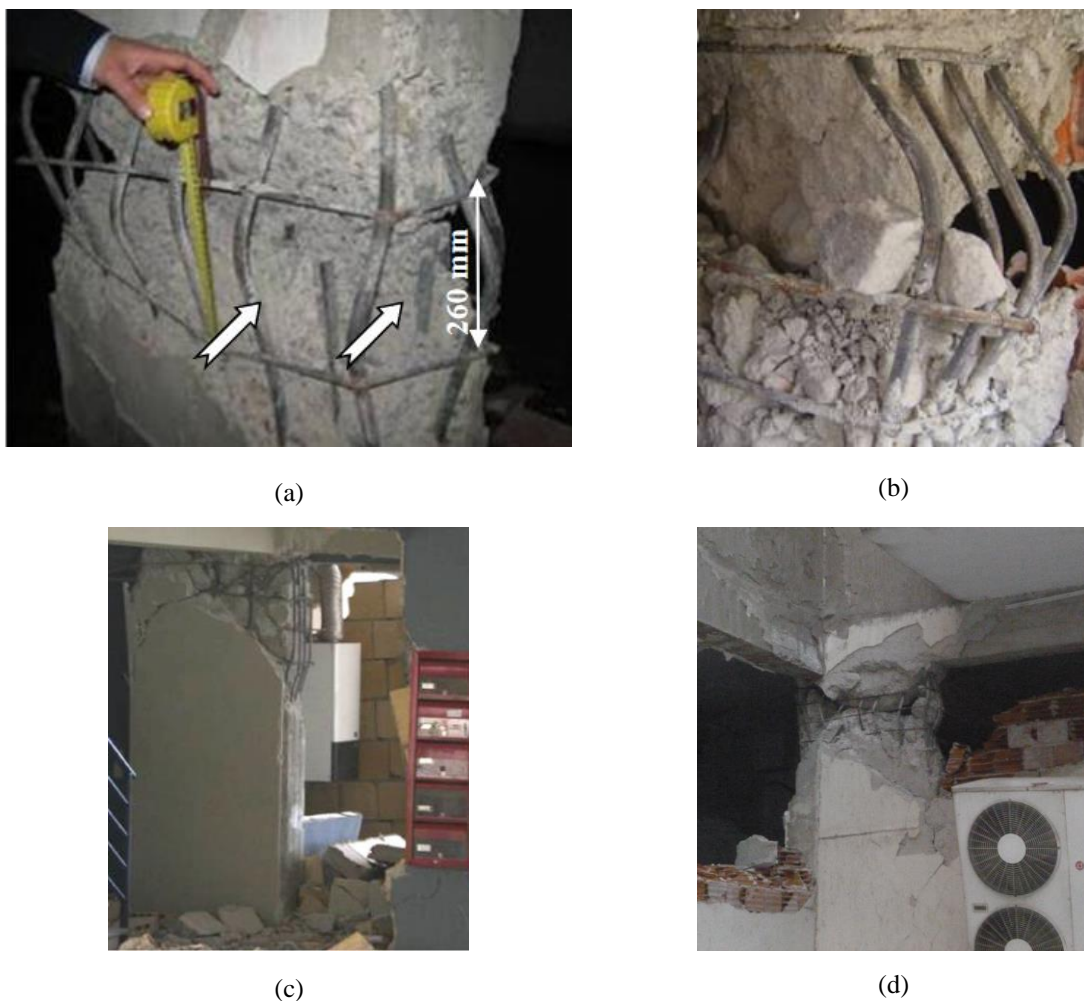


Fig. 1.15. Column axial failure (a) Van 2011 earthquake, Turkey (Öztürk 2015) (b) Kütahya-Simav 2011 earthquake (Yılmaz and Avşar 2013) (c) L'Aquila 2009 earthquake, Italy (Ricci et al. 2011) (d) İzmir Seferihisar 2020 earthquake, Turkey (Photo Credit: Özgür Avşar).

### 1.3.2 Strong Beam-Weak Column

To provide the required level of ductility, the plastic hinge should take place in the beam. To this end, the flexural capacity of the column end should be higher than the flexural capacity of

the beam end. In many cases, this phenomenon is violated due to deep/strong beams connected to weak/flexible columns. The plastic hinge forms in the column end, which can result in severe damage or even loss of stability (Fig. 1.16a and b).



(a)



(b)

Fig. 1.16. Strong beam-weak column failure (a) Van 2011 earthquake, Turkey (Öztürk 2015) (b) Kashmir 2005 earthquake, Pakistan (Naseer et al. 2010).

### 1.3.3 Lap Splice (Bond-Slip) Failure

In the conventional approach, the perfect bond between the concrete and reinforcement bar, which provides the required level of interaction, is assumed. However, buildings constructed in the 70s cannot or can barely satisfy fundamental criteria. Besides, the actual overlapping distance is well below the required one, which results in bond-slip failure together with pull-out failure (Fig. 1.17a and b).



(a)



(b)

Fig. 1.17. Reported lap splice failure (a) Çagatay (2005) (b) Elwood (2006).

### 1.3.4 Column Shear Damage

Some of the columns with improper detailing could not resist the large shear demand and attained their shear capacity, causing visible shear cracks on the columns and brittle type of column shear damage (Fig. 1.18). The large stirrup spacing decreased the shear capacity of the columns. In addition, the low-strength concrete has contributed to the shear cracks developed on the columns. Moreover, the aggregate interlock mechanism, one of the primary sources of concrete shear strength, is not sufficient due to the improper gradation of aggregates. Overall, the shear cracks took place at the column members as a result of several deficiencies.

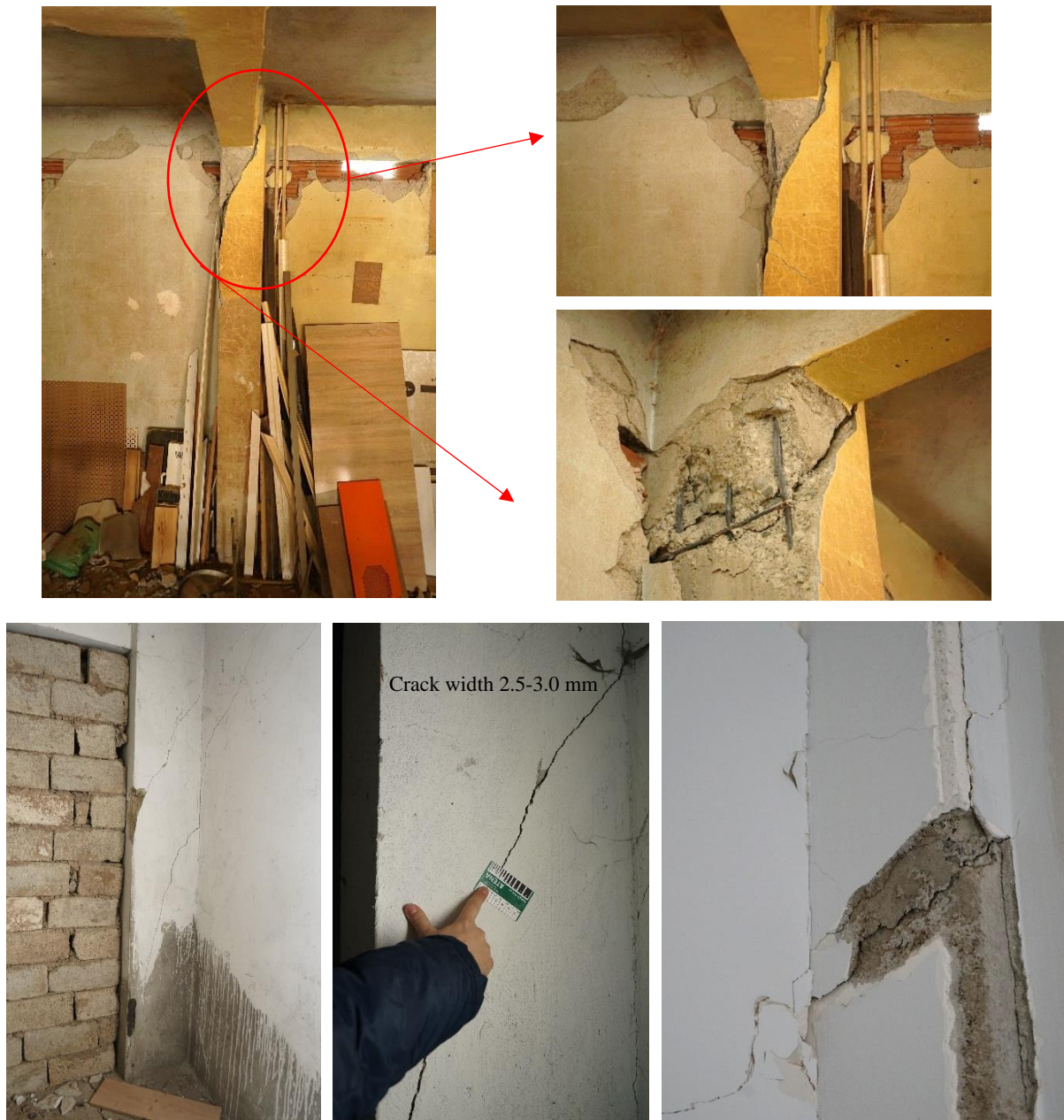


Fig. 1.18. Column shear damage (Yurdakul et al. 2021).

### 1.3.5 Short Column

In many cases, the effective height of the column can be much less than the story height. The reduction in the column's effective height can be due to the structural and non-structural restrictions of the lateral displacement of the columns. The stiffness of such columns increases considerably in proportional to the reduction of column effective height, resulting in an excessive increase in the column shear demand during seismic excitation. When the short column phenomenon is combined with the substandard RC column detailing, the column shear failure is unavoidable, as seen in Fig. 1.19a-c.



Fig. 1.19. Short column due to structural element (a) Elazığ 2020 earthquake, Turkey (Yurdakul et al. 2021) (b) Van 2011 earthquake, Turkey (Öztürk 2015) (c) L'Aquila 2009 earthquake, Italy (Ricci et al. 2011).

### 1.3.6 Captive Column

The restricted column lateral displacement can also reduce the column's effective height due to the non-structural components. Such a phenomenon called the captive column is generally observed in columns adjacent to ribbon windows (Fig. 1.20). If the infill wall beneath the ribbon window has sufficient strength and stiffness to restrict the lateral displacement of the column, the effective height of the column is reduced to the height of the ribbon window. Therefore, shear demand on the captive columns increases tremendously as a result of its increased lateral stiffness. When the shear capacity of the captive column is not sufficient to resist the increased shear demands, column shear failure becomes inevitable.



Fig. 1.20. Captive column due to ribbon window (Yurdakul et al. 2021).

### 1.3.7 Accidental Captive Column

The brittle shear damage can be observed in some of the columns interacting with the infill wall. The damage pattern in the column is formed with the same phenomenon in captive or short column damage (i.e., brittle-type shear damage). However, the frames of such columns have masonry infill walls without any openings. The shear damage at columns similar to the short or captive column damage can be seen in Fig. 1.21a and b. Although the captive columns are not expected for columns of frames having infill walls without openings, severe shear cracks were observed as in the cases shown in Fig. 1.21a and b. The corner region of the infill walls crushes due to the excessive axial load developed in the diagonal struts, while the lower parts of the infill wall below the corner region are intact. The upper part of the column, which is in contact with the corner region of the infill crushed locally, can displace laterally. On the other hand, the lateral displacement of the rest of the column is restricted by the diagonal struts developed in the lower part of the infill. Reducing the unsupported length of the column increases the shear demand. If the strength of the diagonal strut developed on the infill wall is greater than the shear strength of the column, then the brittle type of column shear failure is very likely, as in the case of captive columns. Note that the seismic response of the corresponding frames is affected by the material and geometric characteristics of the infill walls and columns. Therefore, in RC buildings with low-strength concrete, reinforcement with improper detailing, and infills with good quality (strength of infill units, mortar, and plaster is good), accidental captive column damage is highly probable.



(a)



(b)

Fig. 1.21. Accidental captive column (a) Elazığ 2020 earthquake, Turkey (Yurdakul et al. 2021) (b) İzmir Seferihisar 2020 earthquake, Turkey (Photo Credit: Özgür Avşar).

## 1.4 Repairability of RC Columns

Depending on the damage level, RC buildings and their structural components that exhibited moderate to severe structural damage should be repaired or demolished. A comprehensive literature review of codes, standards, guidelines, and relevant scientific studies (FEMA P58 2018; FEMA 306 1998; ESM 98 1998; JBDPA 2001; fib Bulletin No. 25 2003; JRC 2007; Nakano et al. 2004; Cardone 2016; HAZUS MR4 2003; Mergos and Kappos 2013) for the reparability of RC columns is summarized in [Table 1.1](#). The damage state in the RC column is defined by the damage level (DL) characterizing the severity and extent of the macroscopic damage at the RC members or building. According to recognized literature (FEMA 306 1998; JRC 2007; FEMA P58 2018), the damage indicators are classified into five groups. Then, the corresponding damage classification belonging to available codes, guidelines, or relevant studies is paired with identical damage levels. It is worth noting that the association of the damage classification to a specific damage level may have significant differences depending on the considered reference document. An extensive overview of available literature on damage classification is conducted to select the most reliable damage classification. The qualitative definitions of damage levels indicated in recognized literature (FEMA 306 1998; JRC 2007; FEMA P58 2018) are as follows:

- Damage Level 1 (DL1) represents negligible to slight damage (e.g., cosmetic damage) on the RC member with hairline cracks. Finishing work is required for structural members.
- Damage Level 2 (DL2) corresponds to slight structural damage. The intensity of damage is light and visible cracking of concrete can be observed on structural members. The crack widths are wide enough for epoxy injection with no further repair action.
- Damage Level 3 (DL3) is associated with the apparent macroscopic damage at RC components. They are graded as moderately damaged, and the building is uninhabitable. The wide cracks, the onset of concrete spalling, and the local concrete crushing are expected at DL3. The capacity and stiffness of the component can be restored by proper repair action (i.e., epoxy injection and concrete patching).
- Damage Level 4 (DL4) indicates heavy damage at members. Severe shear/flexural damage or even partial collapse of a few members could be encountered. The repair action requires a massive reconstruction and intrusive repair procedures.

- Damage Level 5 (DL5) denotes the very heavy damage at RC members and the incipient collapse of the structure. Severe damage at members, concrete crushing, reinforcement buckling, significant reduction at member resistance, leaning of the building, and loss of stability are expected in this damage level. Realizing a repair is very difficult, time-demanding, costly, and not practical.

Table 1.1. Summary of damage levels and corresponding repair actions.

Damage level	Notes	EMS 98 (1998) (building level)	FEMA 306 (1998) (shear walls)	JBDPA (2001) (columns and walls)	fib Bulletin No.25 (2003) (columns)	AeDES (JRC 2007) (columns)	FEMA P58 (2018)		Nakano <i>et al.</i> (2004) (columns)	Cardone (2016) (ductile weak columns)	Mergos and Kappos (2013) (columns)	HAZUS MR4 (2003) (for pre-code frames)
							Building level (DS for residual capacity)	Non-conforming weak columns				
DL1	Definition	Grade 1: Negligible to slight damage (no structural damage)	Null damage	Visible narrow cracks on concrete surface	Cosmetic (No structural damage)	D0: No damage	DS0	Cosmetic (no structural damage)	Narrow cracks	Null damage	Null	None
	Imposed drift											
	Residual drift											
	Maximum crack width											
	Residual crack width			<0.2 mm	<1.0 mm				<0.2 mm			
Notes on repairability								Repair of finishing				
DL2	Definition	Grade 2: Moderate damage (slight structural damage)	Minor	Visible clear cracks on concrete surface	Onset of cracking due to lateral effects	D1: Slight damage	DS1	DS0	Visible cracks	Light cracking	Minor damage	Slight structural damage
	Imposed drift							1.5%				0.40%
	Residual drift						0.2%					
	Maximum crack width											
	Residual crack width	Cracks in columns and beams of frames	<1.6 mm	>0.2 mm <1.0 mm	>1.0 mm <3.0 mm	<0.5 mm		<1.5 mm	>0.2 mm <1.0 mm	<1.0-1.5 mm	<2.0 mm (flexural) <2.0 mm (bond) <0.5 mm (shear)	Hairline cracks
Notes on repairability				Epoxy injection			Epoxy injection		Epoxy injection			
DL3	Definition	Grade 3: Substantial to heavy damage (moderate struct. damage)	Moderate	Remarkable wide cracks, local concrete crushing	Crushing and spalling of concrete	D2-D3 medium-severe damage	DS2	DS1	Remarkable wide cracks	Onset of concrete spalling	Moderate damage	Moderate structural damage
	Imposed drift							2.0%				0.60%
	Residual drift						0.5%					
	Maximum crack width											
	Residual crack width	Cracks in columns and beam-column joints	<3.2 mm	>1.0 mm <2.0 mm	>3.0 mm	<2-3 mm		>1.5 mm	>1.0 mm <2.0 mm	>3.0 mm <5.0 mm	Spalling (flexure) >2.0 mm (bond) >0.5 mm (shear)	Larger shear cracks and spalling
Notes on repairability					Too wide for epoxy injection			Threshold for economic feasibility of repair		Replacement of spalled concrete		

Table 1.1 (cont.). Summary of damage levels and corresponding repair actions.

	Definition	Grade 4: Very heavy damage (heavy structural damage)	Heavy	Remarkable crush of concrete	Reinforcement buckling	D4: very heavy damage and/or collapse	DS3	Spalling of concrete	Spalling of concrete	Onset of concrete crushing	Severe	Extensive structural damage
	Imposed drift							2.5%				1.60%
	Residual drift					1-2%	1%					
DL4	Maximum crack width											
	Residual crack width	Large cracks in structural elements	>3.2 mm <9.5 mm	>2.0 mm		>3.0 mm			>2.0 mm		Crushing (flexure) Fix-end and pull-out related cracks (bond) >1 mm (shear)	Shear/bond failure, partial collapse
	Notes on repairability	Collapse of a few columns				Limit of partial collapse of the main structural components	Repair may not be economically feasible	Repair may not be economically feasible	Remarkable crush with exposed reinforcing bars	Remove and recast concrete portions		
	Definition	Grade 5: Destruction (very heavy structural damage)	Extreme	Visible settlement and/or leaning of the building	Loss of gravity load capacity	D5: total collapse	DS4	Concrete core crushing	Loss of stability	Null	Null	Complete structural damage
	Imposed drift							3.22%				4.00%
	Residual drift						1-4%					
DL5	Maximum crack width											
	Residual crack width			Cracks in core concrete								
	Notes on repairability	Collapse of ground floor or parts of buildings				Total collapse of the main structural components	Repair may not be economically feasible	Repair may not be economically feasible				Loss of frame stability

## 1.5 Research Objective and Scope

The current study proposes a feasible repair strategy for heavily damaged [i.e., axial failure with significant bond] RC columns by CFRP. Within the content of this study, the experimental responses of both as-built and repaired RC columns are investigated, which is achieved for all specimens through laboratory tests and experimentally validated numerical models.

This study mainly aims to investigate the efficiency of an advanced material (i.e., CFRP) as a repair strategy. The deficient RC columns with low-strength concrete, plain round bars, and improper reinforcing schemes are selected to be representative of the building inventory in both developed and developing countries. The specimens first expose to cyclic action, then the pre-damaged specimens are repaired by CFRP. Those are tested again under the same loading action, and the performance of as-built and repaired specimens are compared.

Another objective of the current research program is to generate an experimentally validated numerical model of all specimens. Thus, the experimental response of the specimens is not only well-characterized by the numerical model, but also the stress/strain development and cracking patterns are adequately reproduced in the FE environment. This provides insight into details that cannot be revealed in the tests.

Given the aforementioned information, the basic premises of this study, in the order of the conducted methodology, can be summarized as follows:

- i. Examining the experimental performance of full-scale substandard RC columns with combined failure modes (i.e., axial failure with significant bond deterioration) imposed by cyclic loading.
- ii. Developing a repair action after severe damage (i.e., repair strategy) by the use of advanced material, i.e., CFRP.
- iii. Validating the numerical models against the experimental performance.

## 1.6 Manuscript Organization

This research context is organized into five main chapters. The output of the study and its context are presented in this chapter, while the next chapters are introduced as follows:

Chapter 2 presents the experimental program. The details such as the design of specimens, test setup, instrumentation, and loading procedure are comprised as well. The design methodology for CFRP-repaired columns is also included in this chapter.

Chapter 3 deals with the numerical modeling approach. A general view of numerical modeling techniques is included in this chapter. A summary of available material models for the compressive/tensile behavior of concrete, yield/failure functions for concrete material, reinforcing material models, FRP material, and interface models are presented.

Chapter 4 presents the exhibited experimental performance of as-built and CFRP-repaired RC columns. The hysteric behavior and the response parameters of prime interest are summarized in this chapter. The effectiveness of numerical models (i.e., comparison with experimental response) is included as well.

Chapter 5 deals with concluding remarks drawn from this study and the summary of the habilitation thesis.

# 2

## EXPERIMENTAL PROGRAM

---

### 2.1 Specimen Design

The cantilever column with a single curvature response is taken from the theoretical inflection point of the RC frame, where the moment is zero under lateral load. The flexural response with significant bond degradation and axial failure is the target failure mode, which is also observed by the author on field inspections after damaging earthquakes (see Chapters [1.3.1](#) and [1.3.3](#)). Therefore, actual site conditions to reach the target failure mode are imitated in the manufactured specimens. The full-scale test specimens, representing the RC column with single footing, are constructed by considering the most common deficiencies. The basic geometrical and material parameters of ordinary pre-70s structures with substandard configuration are summarized in Chapter [1.2](#). In dimensioning and detailing the tested RC column specimens, the presented common parameters and existing deficiencies for ordinary pre-70s structures (i.e., low-strength concrete, plain round bar, and improper reinforcing scheme) are considered ([Table 2.1](#)).

Table 2.1. Target geometrical and material parameters retrieved from available literature.

Parameter	Literature (Chapter 1.2)		Current Study	Remarks
	Mean $\mu$	Coefficient of variation $C_v$		
Story height [m]*	2.87	0.10	3.00	Single curvature test of cantilever column with a height of 1.75 m (1.50 m at loading point-story height 3.00m)
Column width [mm]*	255	0.08	350	A symmetrical column is adopted
Column depth [mm]*	535	0.25	350	
Longitudinal reinforcement steel ratio*	0.96-1.14%	0.12-0.33	1.00%	Minimum in EN 1992-1 (CEN 2004a): 1.00%
Reinforcing steel yield strength [MPa] <sup>+</sup>	371.10	0.24	275	Plain round bar
Transverse reinforcement diameter [mm]*	8.00	0.02	8.00	Plain round bar, closed hoop with 90° hook
Transverse reinforcement spacing [mm]*	181.21	0.20	150	Selected according to construction practices
Lap splice <sup>c</sup>	50d <sub>b</sub>	N/A	50d <sub>b</sub>	Obtained from the investigated blueprints
Concrete compressive strength [MPa]	10.64 <sup>#</sup> 16.73 <sup>+</sup>	N/A <sup>#</sup> 0.51 <sup>+</sup>	Table 2.2	Low-strength concrete with improper mix-design, poor compaction and segregation
Axial load ratio [ $N/A_c f_c$ ] <sup>c</sup>	0.32	0.53	0.32 and 0.15	Based on the 284 observations in the buildings located in İstanbul, Turkey. Mean value for high axial load ratio, $\mu = 0.32$ Lower boundary of the prominent range referring to low axial load ratio, $\mu - \sigma_r = 0.15$

\*Ozmen et al: (2015), <sup>+</sup>Bal et al. (2008), <sup>#</sup>Mazilıgüney et al. (2008), and <sup>c</sup>Current study

Three different reinforcing schemes are used (Fig. 2.1a-c). The first group of columns is constructed with continuous longitudinal bars without lap-splice length (Fig. 2.1a). The second group refers to confirming configuration with sufficient lap-splice length and hooks at the ends of the plain reinforcing steel (Fig. 2.1b). The third reinforcing scheme is a non-conforming configuration without hooks (Fig. 2.1c). Note that the continuous reinforcing steel without lap-splice (Fig. 2.1a) does not represent the actual detailing configuration; in turn, the theoretical considerations assume a perfect connection at a lap-splice distance. Those are also summarized in Table 2.2.

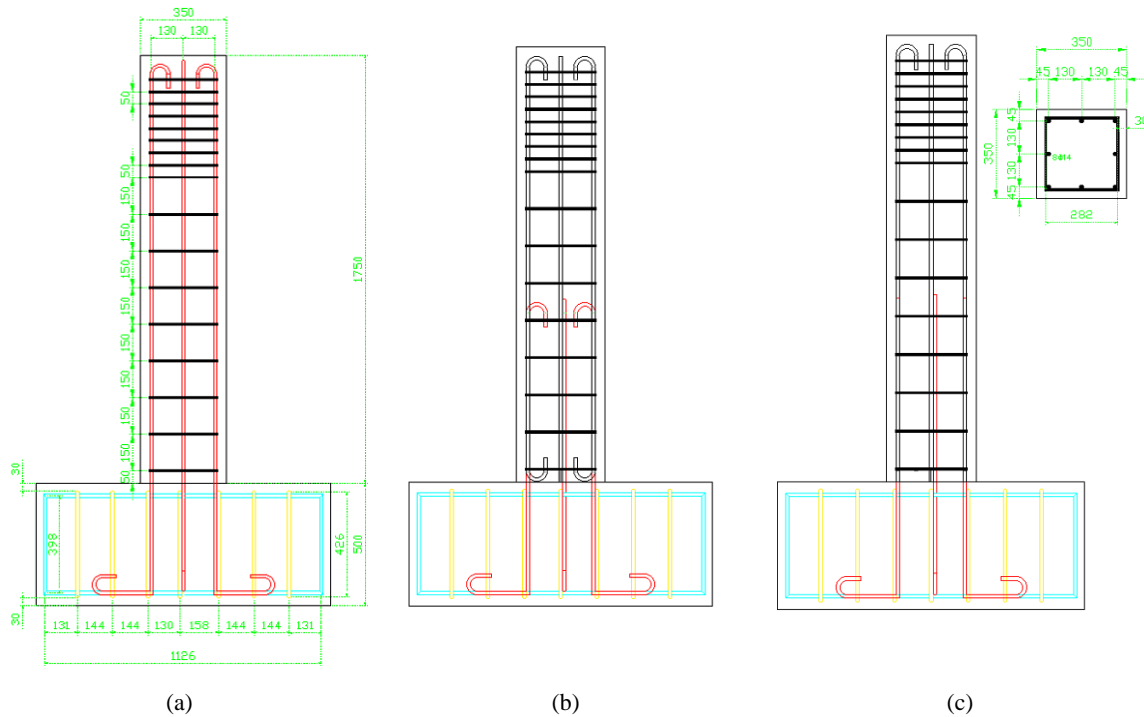


Fig. 2.1. Reinforcement scheme (a) continuous without lap-splice length (b) confirming configuration with hooks (c) non-conforming configuration without hooks.

To establish the relative effect of high and low axial load, two levels of axial load ratio  $\sigma_n$  are implemented. Note that the mean value  $\mu$  of axial load ratio  $\sigma_n$  is 0.32 in the analyzed buildings (see Chapter 1.2.2.4). The standard deviation  $\sigma_r$  is computed as 0.17. The mean value of the statistical data refers to a high axial load ratio (0.32) in this study. Since the axial load contributes to the bond performance, the lower axial load ratio is assumed, which is the lower boundary of the prominent range of the statistical data (i.e.,  $0.15.; \mu - \sigma_r$ ). The summary of specimens can be seen in Table 2.2.

## 2.2 Test Setup, Procedure, and Instrumentation

In the test, the cantilever column with a total height of 1.75 m (2.25 m with footing) is positioned vertically and fixed to a strong floor. Two actuators with a capacity of 630 kN, at which constant axial load is applied, are fixed to the beam of the loading frame. The lateral displacement with increasing amplitude is applied by the actuator with a capacity of 250 kN, which is fixed to the loading column through hinges and rigid steel plates. Moreover, the out-of-plane movement of specimens is restricted by supporting the loading beam laterally (Fig. 2.2).

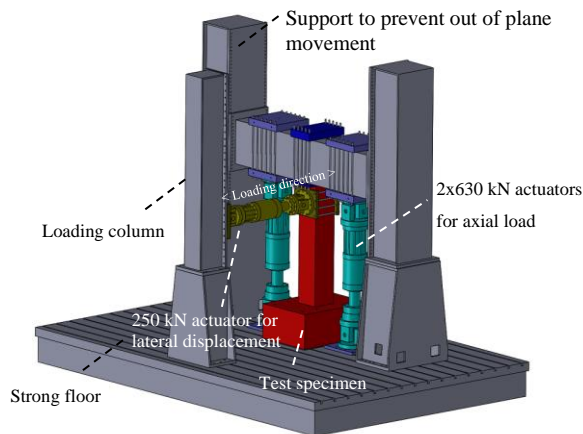


Fig. 2.2. Test setup.

The intensive level of the damage is simulated by the imposed quasi-static cyclic displacement, which is carried out up to specified displacement levels (Fig. 2.3). FEMA 461 (2007) is the guiding document for the displacement protocol, which may be implemented for drift-sensitive structural and nonstructural components. Two cycles with a loading speed of 1 mm/s are imposed in each loading amplitude not to induce any dynamic effects during the testing. It should be emphasized that the notified drift ratio represents the ratio of measured lateral displacement to column height (i.e., 1.50 m). The displacement pushing the column tip represents the positive loading direction, while the negative loading direction is achieved when pulling the specimen.

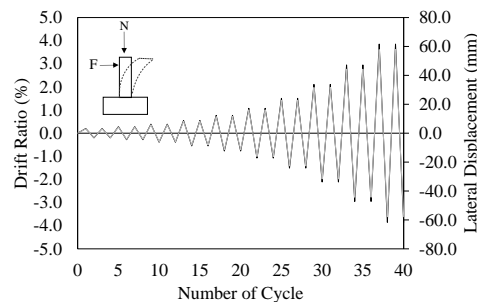
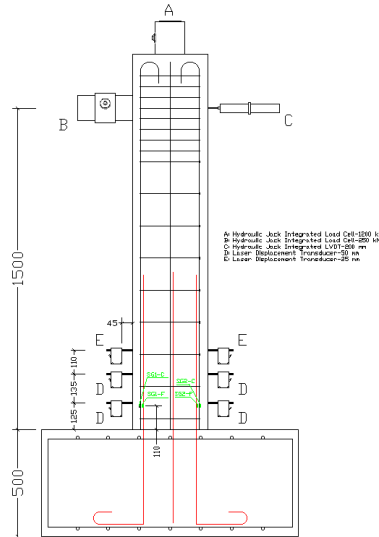


Fig. 2.3. Displacement history.

The hydraulic actuator-integrated linear variable differential transducer (LVDT) measures the column tip displacement. Simultaneously, the hydraulic actuator-integrated load cells record the lateral force (i.e., column shear) along with the constant column axial force. Contactless laser displacement transducers monitor the column base deformation. The strain gauges are placed in the half Wheatstone bridge configuration to the reinforcing steel to measure the strain at different displacement levels. All data from the measuring tools are recorded by dynamic data acquisition simultaneously. The position of the sensors is depicted in Fig. 2.4.



Dimensions in mm

Fig. 2.4. Instrumentation on specimens.

## 2.3 Repair Design

The design philosophy in rehabilitating RC specimens is to attain the initial capacity, upgrade the performance of structural members, delay or eliminate brittle failure modes, and initiate the formation of flexural plastic hinges to attain a ductile behavior (El-Amoury and Ghobarah 2002). In dimensioning CFRP sheets, such a philosophy is implemented in four different approaches: (i) flexural strengthening; (ii) shear strengthening; and (iii) ductility strengthening.

### 2.3.1 Flexural Strengthening

In the flexural design, the contribution of the existing longitudinal bars is neglected. It was assumed that the ultimate longitudinal force in the reinforcing steel would be carried only by the corresponding CFRP sheets while other premature failures were prevented. The contribution of CFRP to flexural strength  $V_{frp,F}$  is evaluated according to Eq. (2-1). Note that  $V_{frp,F}$  should be equal to- or higher than the ultimate longitudinal force in the reinforcing steel exerted during the test. Since the test results are known, it is computed accordingly. If not, the section analysis can be performed to find corresponding forces in the reinforcing steel.

$$V_{frp,F} = n_f w_f t_f E_f \varepsilon_{fe} \quad \text{Eq. (2-1)}$$

Here,  $n_f$  is the number of CFRP layers,  $w_f$  is the width of the CFRP layer,  $t_f$  is the thickness of the CFRP layer,  $E_f$  is the elastic modulus of the CFRP layer, and  $\varepsilon_{fe}$  is the effective strain described in ACI 440.2R-17 (2017) for flexural strengthening, which is:

$$\varepsilon_{fe} = \varepsilon_{cu} \left[ \frac{d_f - c_s}{c_s} \right] - \varepsilon_{bi} \leq \varepsilon_{fd} \quad \text{Eq. (2-2)}$$

where  $\varepsilon_{cu}$  ultimate compressive strain,  $d_f$  effective depth of FRP,  $c_s$  is the distance from extreme compression fiber to the neutral axis,  $\varepsilon_{bi}$  initial strain of bonded substrate, which can be determined from elastic analysis, and  $\varepsilon_{fd}$  debonding strain, which is defined as:

$$\varepsilon_{fd} = 0.41 \sqrt{\frac{f_c}{n_f E_f t_f}} \leq 0.9 \varepsilon_{fu} \quad \text{Eq. (2-3)}$$

where  $\varepsilon_{fu}$  is the ultimate FRP strain while other parameters are defined above.

### 2.3.2 Shear Strengthening

In the shear design, the contributions of the existing shear reinforcement and concrete are neglected. It is assumed that the required additional shear strength  $V_{frp, required}$  is assumed to be equal to the experimental column shear force  $V_c$ . If experiment results are not available, the result from analytical or computer analysis can be used.

Following ACI 440.2R-17 (2017), the required FRP layer can be computed.

$$V_{frp, required} = \frac{V_c}{\phi_s \psi_f} \quad \text{Eq. (2-4)}$$

where  $V_c$  experimental column shear,  $\phi_s$  is the safety factor; 0.85, and  $\psi_f$  is the strength reduction factor; 0.95. The contribution of FRP to shear strength  $V_{frp, s}$  is computed following ACI 440.2R-17 (2017).

$$V_{frp, s} = \frac{A_{fv} E_f \varepsilon_{fe} (\sin \alpha + \cos \alpha) d_{f, s}}{s_f} \quad \text{Eq. (2-5)}$$

where  $E_f$  is the elastic modulus,  $\varepsilon_{fe}$  is the effective strain, which is  $0.004 \leq 0.75 \varepsilon_{fu}$  according to ACI 440.2R-17 (2017), (here,  $\varepsilon_{fu}$  is the rupture strain of CFRP),  $\alpha$  is the angle of FRP sheet (see Fig. 2.5),  $d_{f, s}$  is the height of FRP from end to the center of longitudinal reinforcement level (see Fig. 2.5), and  $A_{fv}$  for rectangular sections is as follows.

$$A_{fv} = 2n_f w_f t_f \quad \text{Eq. (2-6)}$$

The other variables are defined in the previous section, while some are also visually presented in Fig. 2.5.

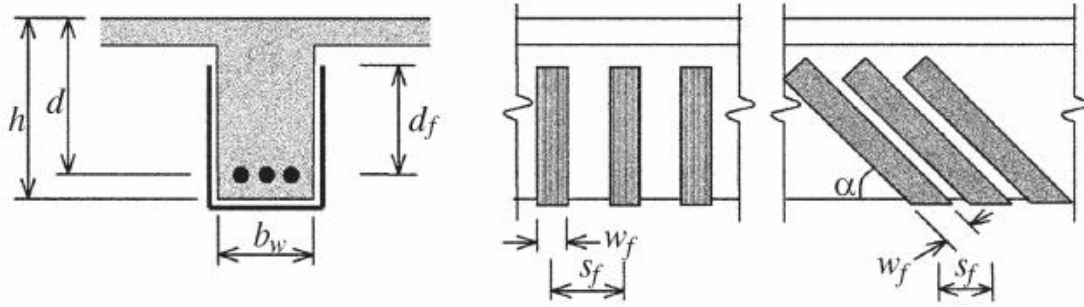


Fig. 2.5. Illustration of the dimensional variables used in shear-strengthening calculations for repair, retrofit or strengthening using FRP laminates (figure from ACI 440.2R-17 (2017)).

### 2.3.3 Ductility Enhancement

More complex calculations to determine the capability of a member to sustain rotation and drift without a substantial loss in strength are required. The observed ductility of tested RC columns should be restored. To do so, the required number of FRP layers should confine the plastic hinge region. Following ACI 440.2R-17 (2017) procedure, the displacement ductility can be obtained as follows:

Step 1- Obtain the yield and ultimate curvature, and corresponding moments from moment-curvature ( $M-\phi$ ) analysis for a completely wrapped section with  $n$  transverse plies, where  $n$  is the number of layers.

Yield curvature  $\phi_{y,frp}$ , ultimate curvature  $\phi_{u,frp}$  and corresponding yield moment capacity  $M_{y,frp}$ , ultimate moment capacity  $M_{u,frp}$

Step 2-Compute the displacement ductility  $\mu_d$ .

Step 2.1-Obtain plastic hinge length  $L_p$

For FRP retrofitted members, refer ACI 440.2R-17 (2017)

$$L_p = g + 0.044f_y d_b$$

where  $d_b$  is the diameter of the flexural steel,  $f_y$  is the yield stress of flexural steel, and  $g$  is the clear gap between the FRP jacket and adjacent members.

Step 2.2-Obtain the effective length  $L_{eff}$

For single curvature,  $L_{eff} = L$

For double curvature,  $L_{eff} = L/2$

where  $L$  is specimen height.

Step 2.3-Obtain the yield deflection  $\Delta_{y,frp}$

$$\Delta_{y,frp} = \frac{\phi_{y,frp} L_{eff}^2}{3}$$

Step 2.4-Obtain the plastic deflection  $\Delta_{p,frp}$

$$\Delta_{p,frp} = (\phi_{u,frp} - \phi_{y,frp}) L_p \left( L_{eff} - \frac{L_p}{2} \right)$$

Step 2.5-Obtain the displacement ductility  $\mu_d$

$$\mu_d = 1 + \left( \frac{\Delta_{p,frp}}{\Delta_{y,frp}} \right)$$

The steps can be repeated by changing the FRP layer in the section analysis until the target displacement ductility  $\mu_d$  is achieved.

### 2.3.4 Anchor Design

The transverse wraps anchor the longitudinal FRP placed for flexural strengthening in the column. The longitudinal FRP is extended to the footing and anchored to the footing by FRP fiber anchors. The development length of FRP in footing (i.e., extension of FRP from column to footing) is approximated to ACI 440.2R-17 (2017) proposal, which is as follows:

$$l_{df} = \sqrt{\frac{n_f E_f t_f}{\sqrt{f_c}}} \quad \text{Eq. (2-7)}$$

where  $l_{df}$  is the development length, while other parameters are described in previous sections.

The design anchor length of FRP fiber anchors for anchoring the extended FRP to the footing is assumed to be the same as the bond of near-surface mounted systems which is in accordance with ACI 440.2R-17 (2017).

$$l_{ab} = \frac{d_{ba}}{4\tau_b} f_{fd} \quad \text{Eq. (2-8)}$$

where  $l_{ab}$  is anchor length,  $d_{ba}$  is the diameter of the fiber anchor,  $f_{fd}$  is the design axial stress in the anchor, and  $\tau_b$  is the bond stress, which is equal to 6.9 MPa according to ACI 440.2R-17 (2017).

## 2.4 Structural Repair

MAPEI company supports the current research program by providing CFRP material and passive technical support. Therefore, the MAPEI CFRP and its related products are used. Following the previous chapter, the weight of CFRP per  $m^2$  is dimensioned. 2 layers of 300  $g/m^2$  CFRP in the longitudinal direction and 1 layer of 300  $g/m^2$  CFRP in the transverse direction is used. The longitudinal CFRP is used to recover the flexural capacity. The pull-out failure due to extensive slip of the plain round bar is prevented as well. The part of the longitudinal CFRP layers extended to the foundation is anchored by CFRP fan anchors to the foundation. CFRP layers in the lateral direction help to increase shear capacity and displacement ductility with provided confinement pressure. Those also anchor the longitudinal CFRP layers. After finding the required level of CFRP, the step-by-step description of the structural repair is visually presented in [Fig. 2.6](#).



Step 1-Unloading the specimen from test-setup



Step 2-Removing the loose concrete



Step 3-Formwork for repair mortar



Step 4-Applied repair mortar



Step 5-Rounding column-foundation interface



Step 6-Rounding sharp corners on column



Step 7-Crack filling by epoxy injection



Step 8- Wet epoxy resin application for fiber anchor



Step 9-Sanding fiber anchor



Step 10-Primer application



Step 11-Putty concrete application



Step 12-Dry epoxy resin application



Step 13-CFRP sheet wrapping



Step 14-Chemical anchor for fiber anchors



Step 15-Final product

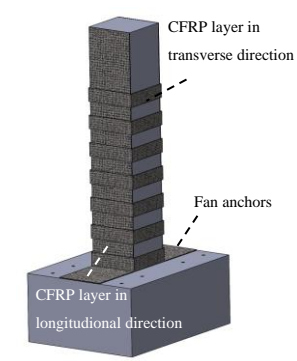


Fig. 2.6. Repair of RC column by CFRP.

Table 2.2. Details of tested specimens.

Parameter	Specimen											
	E1-NC-L	E1-NC-H	E1-C-L	E1-C-H	E1-T-L	E1-T-H	E1-NC-L-R	E1-NC-H-R	E1-C-L-R	E1-C-H-R	E1-T-L-R	E1-T-H-R
Configuration	Fig. 2.1c	Fig. 2.1c	Fig. 2.1b	Fig. 2.1b	Fig. 2.1a	Fig. 2.1a	Reparation of E1-NC-L	Reparation of E1-NC-H	Reparation of E1-C-L	Reparation of E1-C-H	Reparation of E1-T-L	Reparation of E1-T-H
Description	As-built						Repaired after pre-damage following the procedure in Fig. 2.6					
Repair Scheme	N/A						CFRP					
Concrete Compressive Strength $f_c$ [MPa]	12.52	11.95	12.77	11.93	12.46	12.12	Same as E1-NC-L	Same as E1-NC-H	Same as E1-C-L	Same as E1-C-H	Same as E1-T-L	Same as E1-T-H
Column Reinforcement (Plain round bar)	Top					3 $\phi$ 14						
	Intermediate					2 $\phi$ 14						
	Bottom					3 $\phi$ 14						
	Transverse					$\phi$ 8/150						
Lap-Splice	50db	50db	50db	50db	No Lap-Splice	No Lap-Splice	Same as E1-NC-L	Same as E1-NC-H	Same as E1-C-L	Same as E1-C-H	Same as E1-T-L	Same as E1-T-H
Footing	900 x 1200 x 500 mm											
Column Cross-Section	350 x 350 x 1750 mm											
Axial Load Ratio ( $\sigma_n=N/A_c f_c$ )	0.15	0.32	0.15	0.32	0.15	0.32	0.15	0.32	0.15	0.32	0.15	0.32
Application of Displacement	Single Curvature Column Test-Column Tip											
Loading Protocol	2 Repetition per Cycle (FEMA 461 2007)											
Failure Mode	Bond-slip/Axial Failure	Bond-slip/Axial Failure	Bond-slip/Axial Failure	Bond-slip/Axial Failure	Bond-slip/Axial Failure	Bond-slip/Axial Failure	Flexure/ FRP Debonding	Flexure/ FRP Debonding and Fracture	Flexure/ FRP Debonding	Flexure/ FRP Debonding and Fracture	Flexure/ FRP Debonding	Flexure/ FRP Debonding and Fracture

C: Conforming hook detail

NC: Non-conforming hook detail

T: Continuous reinforcing steel without lap-splice

L: Low axial load

H: High axial load

# 3

## NUMERICAL STUDY

---

As computer-aided nonlinear analysis is now available for RC members, refined numerical models allow for reproducing the response of substandard members with satisfactory accuracy. This chapter briefly presents the numerical modeling strategies in a user-friendly computer tool ATENA software (ATENA Program Documentation, Part 1 2014), used for reproducing the response of RC column with combined failure modes (i.e., bond failure with flexural and axial damage). As reproducing the premature failure of substandard RC columns in the FE environment is often challenging, the knowledge of the current state of modeling strategies is included in this chapter. Moreover, the modeling strategies, theory, and material constitutive laws are discussed in depth. All numerical models are then verified by the experimentally obtained responses.

### **3.1 Numerical Model Description**

The geometry of RC members was defined by the hexahedral element (*CCIsoBrick*). The reinforcement was defined by a 1D beam element. The FE model was created by assembling all parts, which include 1D reinforcing elements, a 3D column base and a 3D column with fracture/plastic material properties, and 3D loading/support plates with elastic material properties. A similar boundary condition of the experiment was assigned in the numerical solution. Generating the optimum FE model is essential to optimize the FE solution because it is fairly sensitive to convergence, computational time, and accuracy. A mesh with a size of 35

mm was found as an optimum. The displacement was applied to an elastic plate as loading from the concrete geometry results in divergence issues. The standard Newton-Rapson method was used for solving the numerical problem. 30 iterations were performed in each loading step. error tolerances were 0.015, 0.015, 0.015 and 0.015 for displacement, residual, absolute residual, and energy error tolerances, respectively.

## 3.2 Material Constitutive Laws

### 3.2.1 Concrete

The concrete geometry was modeled by the hexahedral element *CCIsoBrick*. The constitutive models of tensile (fracturing) and compressive behavior were combined in *CC3DNonLinCementitious2* (a fracture-plastic concrete model) in the software. The compressive strength of the concrete  $f_c$  was obtained in a material test. The remaining modeling parameters were derived from the compressive strength  $f_c$ . To define the compressive behavior of the concrete, it was referred to Van Mier (1986), who considered the elliptical hardening and linear softening behavior (Fig. 3.1a and b). The hardening part is strain-based, whereas the linear softening part considers the plastic displacement  $w_d$ . The relation between deformation (i.e., plastic displacement  $w_d$  under compression and crack opening at full stress release  $w_c$ ) and strain  $\varepsilon$  was obtained by crack band theory (Bazant and Oh 1983). The deformation  $w$  is defined as  $w = \varepsilon L_t$ , where  $L_t$  is the size of the element corresponding to the projection of the element perpendicular to the crack direction. A relation in a form of Gauss's function was adopted to describe the reduction of compressive strength in the cracked concrete. The parameters were derived from the experimental data published by Kollegger and Mehlhorn (1988), which also includes the test data of Vecchio and Collins (1986) (ATENA Program Documentation, Part 1 2014). The strength reduction factor  $c$  in the cracked concrete (see Fig. 3.1c) was defined in Dyngeland (1989). Note that no strength reduction was assumed in the uncracked concrete. The compressive strength begins reducing after the cracking event, which occurs under the strain  $\varepsilon_{cr}$  in Fig. 3.1c. The surface sharpness in the failure evolution was controlled by the Menetrey and Willam (1995) failure surface with eccentricity parameter  $e$   $\langle 0.5, 1.0 \rangle$ .

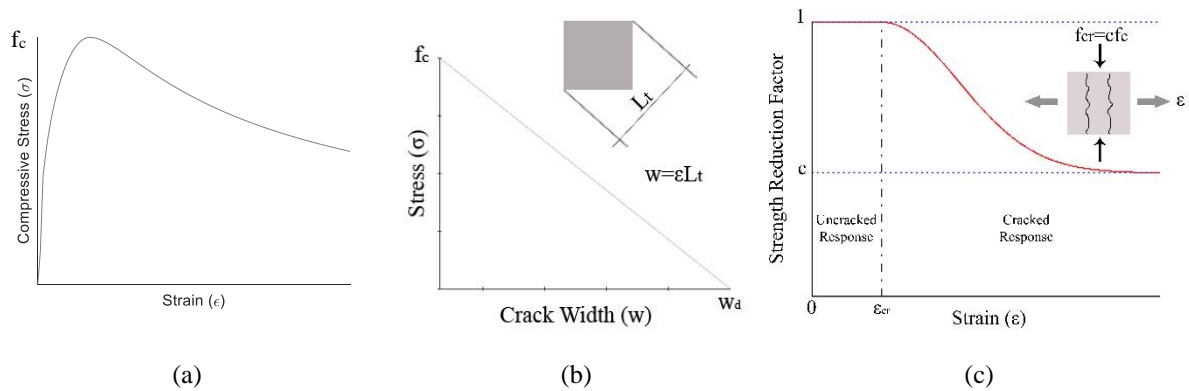


Fig. 3.1. (a) Concrete behavior under compression, (b) Compression softening, (c) Strength reduction in the cracked concrete (ATENA Program Documentation, Part 1 2014).

The tensile behavior of the plain concrete was assumed uncracked in the elastic region. The exponential softening relation between the stress in the crack  $\sigma$  and the crack width  $w$  in the post-elastic region was defined as described in Hordijk (1991). Tension stiffening due to additional strength and stiffness provided by the heavily reinforcement is specified as 40% of the tensile strength of the concrete  $f_{ct}$  following fib (2010) (Fig. 3.2a). The fracture model combined the smeared crack concept with the crack band theory of Bazant and Oh (1983). The software adopted the fixed crack model of Cervenka (1985), which assumes a fixed crack direction after initiation. As the orthotropic and principal strain axes did not overlap, a shear crack developed on the crack face. Concrete cracking was subjected to the Rankine failure criterion (Rankine 1857). The relative effect of aggregate interlock is assumed by defining maximum aggregate size (e.g., 16 mm). The reduction in the shear stiffness after cracking was described following Kolmar (1986). Increasing the strain, which was normal to the crack direction, reduced the shear modulus. The relationship between the reduction in the shear stiffness and the transverse reinforcement ratio was also considered in the model (Fig. 3.2b). All values are summarized in Table 3.1.

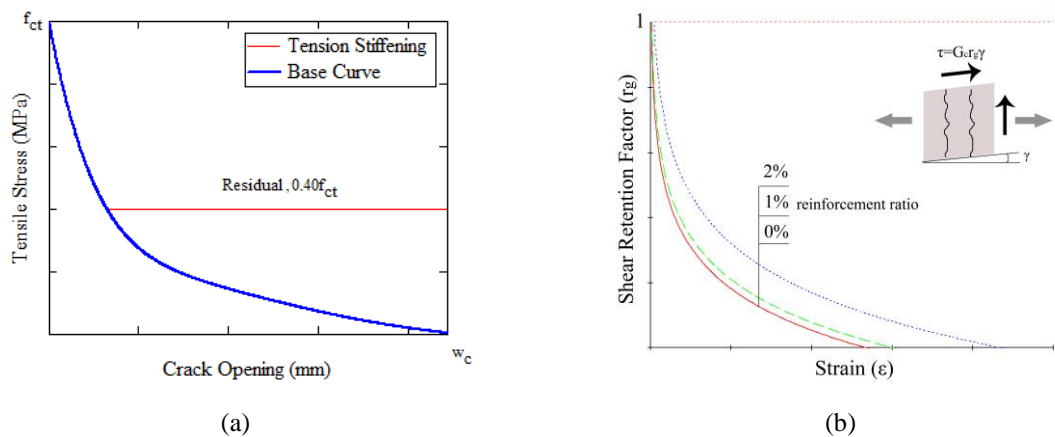


Fig. 3.2. (a) Tension softening and (b) Shear retention factor (ATENA Program Documentation, Part 1 2014).

Table 3.1. Summary of adapted concrete material properties.

Parameter	Value
Compressive Strength, $f_c$ [MPa]	Material Test Results (see <a href="#">Table 2.2</a> )
Compressive Hardening	Elliptical Hardening (Van Mier 1986)
Compressive Strain, $\epsilon_{co}$ [mm/mm]	0.002 (CEN 2004a)
Compressive Softening	Linear (Van Mier 1986)
Plastic Displacement, $w_d$ [m]	Duran <i>et al.</i> (2017)
Compressive Strength Reduction Factor in the Cracked Concrete	Dyngeland (1989)
Elastic Modulus, $E_c$ [MPa]	$f_c/\epsilon_{co}$ (Van Mier 1986)
Tensile Strength, $f_{ct}$ [MPa]	$0.30f_c^{2/3}$ (fib 2010)
Fracture Energy, $G_f$ [N/m]	$73f_c^{0.18}$ (fib 2010)
Tension Softening	Exponential Function (Hordijk 1991)
Tension Stiffening	$0.40f_{ct}$ (fib 2010)
Cracking Criterion	Rankine Failure (Rankine 1857)
Stress in the Crack	Fixed Crack (Cervenka 1985)
Crack Spacing	Crack Band (Bazant and Oh 1983)
Aggregate Interlock	Maximum aggregate size (16 mm)
Shear Modulus Reduction in Cracked Concrete	Kolmar (1986)
Yield Surface	Menetrey and Willam (1995)

### 3.2.2 Reinforcing Steel

The longitudinal reinforcing bars were defined as truss elements in a bilinear elastoplastic model considering the hardening behavior. The Menegotto and Pinto model (1973) for the nonlinear cyclic material behavior of reinforcing steel was employed. The average ultimate strain reached at failure was 40.7 %. However, the strain after reaching the ultimate tensile strength (strains at necking plateau) is neglected. In the bilinear model, the ultimate strain is limited to strain at peak strength, which is 19%. The yielding strain is computed as 0.14%. The measured yield and ultimate strengths in the average sense are 275 MPa and 435 MPa, respectively. Elastic modulus is obtained as 199 GPa. Those were summarized in [Table 3.2](#).

Table 3.2. Summary of adapted reinforcing steel material properties.

Parameter	Value
Elastic Modulus, $E_s$ [GPa]	199
Yield Strength, $f_y$ [MPa]	275
Ultimate Strength, $f_u$ [MPa]	435
Ultimate Strain at Peak Strength, $\varepsilon_o$ [mm/mm]	0.19%
Ultimate Strain, $\varepsilon_u$ [mm/mm]	40.7%
Compressive Behavior	Active
Cyclic Behavior	Menegotto and Pinto (1973)

### 3.2.3 Bond-Slip Model

The reinforcing bar was fully connected to the surrounding concrete geometry with the limited bond strength, which is defined by a *CCBarWithBond* type element. First, the software derives the normal stress in the reinforcing bar. Then, the derivative of normal stress is compared with cohesion stress. If the cohesion stress between the reinforcing bar and surrounding concrete becomes higher than the defined bond stress, the reinforcement bar slips to reduce the stress (ATENA Program Documentation, Part 1 2014). This iterative procedure continues until the solution falls within the defined error tolerances.

For the cyclic response, the bond-model is modified accordingly. When the load started to be exerted in the reverse direction, the slip value did not change considerably. On the other hand, the bond stress changes its sign (Eligehausen et al. 1983; Verderame et al. 2009; ATENA Program Documentation, Part 1 2014). Namely, in the first steps of unloading, the slip value was almost constant while the bond strength changed its sign (i.e., null relative bond). Then, with the increasing slip, bond stress remained almost constant until the reinforcement bar reaches its initial position (i.e., null relative slip). It is henceforth referred to as a semi-circle phenomenon. This model also incorporates the *Memory Bond Material* in ATENA software (ATENA Program Documentation, Part 1 2014). The theoretical relationship in the software considers positive and negative semi-circles during cyclic excitation. The *Memory Bond Material* assumes two different responses for loading and unloading regime. During the loading regime, the software follows the defined bond-slip curve. When bond stress changes its sign (i.e., unloading regime), the model exhibits a semi-circular response for the defined threshold value. The modeling parameters are obtained from the mathematical expression

proposed by the author recently (Yurdakul et al. (2022)), which is visually presented in Fig. 3.3 and mathematically expressed as follows:

$$\tau_c(s) = \begin{cases} \beta_c \times \tau_{c1} \left(\frac{s}{s_{c1}}\right)^{\alpha_b} & \text{if } s < s_{c1} \\ \beta_c \times [0.046s^2 - 0.29s + 0.77]f_c^{1/4} & \text{if } s_{c1} \leq s \leq s_{c2} \\ \beta_c \times \tau_{c2} & \text{otherwise} \end{cases} \quad \text{Eq. (3-1)}$$

where the variables are:

$$\tau_{c1} = 0.60f_c^{1/4} \quad \text{Eq. (3-2)}$$

$$\tau_{c2} = 0.30f_c^{1/4} \quad \text{Eq. (3-3)}$$

$$\alpha = 0.22 \quad \text{Eq. (3-4)}$$

$$s_{c1} = \sqrt{\frac{f_c}{30}} \quad s_{c2} = 3.0 \quad \text{Eq. (3-5)}$$

$$\beta_{c,b} = 0.855e^{f_e/f_c^{2/3}} \text{ for } f_e \geq 0.05 \quad \text{Eq. (3-6)}$$

Bond stress values in MPa  
Slip values in mm

Here, bond strength-related values for confined concrete,  $\tau_{c1}$  and  $\tau_{c2}$ , are the corresponding maximum and residual ones, respectively. Their corresponding slip values are  $s_{c1}$  and  $s_{c2}$ , respectively. The shape factor is defined by  $\alpha_b$  coefficient. The adaptation of the proposed relationship accordingly for different confinement pressure provided by the shear reinforcement is required. Therefore,  $f_e$  and  $\beta_{c,b}$ ; which are effective lateral confinement pressure (in MPa) and confinement factor, respectively; are considered in the bond-slip model for confined concrete. In this study,  $f_e$  is obtained following Mander *et al.* (1988).

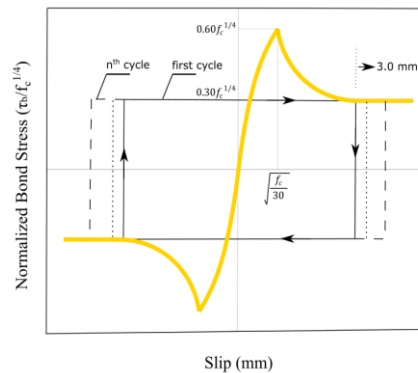


Fig. 3.3. Cyclic bond-slip model for specimens with confinement (Yurdakul et al. (2022)).

### 3.2.4 Cold Joint

Since the footing and column is manufactured in different times, the cold joint phenomenon occurs. Therefore, a perfect contact between footing and column cannot be assumed. It is taken into account by a defined interface between column and footing.

Following fib (2010) and Randl (2013), the shear capacity of the cold joint with dowel action can be computed as follows:

$$\tau_r = \min \left\{ [\beta_c v f_c], [c_r f_c^{1/3} + \mu_c (\sigma_n + \rho \kappa_1 f_y) + \kappa_2 \rho \sqrt{f_c f_y}] \right\} \quad \text{Eq. (3-7)}$$

where  $\beta_c$  is coefficient allowing for angle of diagonal concrete strut (0.4 for smooth surface),

$f_c$  is the concrete compressive strength,

$c_r$  is 0 for smooth surface roughness,

$\mu_c$  is friction coefficient (0.6 for smooth surface),

$\sigma_n$  is the axial load ratio, ( $N/A_c f_c$ ),

$\rho$  reinforcement ratio,

$\kappa_1$  coefficient of efficiency for tensile force (0.5 for smooth surface),

$f_y$  yield strength of the reinforcing steel,

$\kappa_2$  coefficient for flexural resistance of reinforcement (1.1 for smooth surface roughness)

$v$  is reduction factor in strength, which is computed as follows:

$$v = \min \left\{ [0.55], \left[ 0.55 \left( \frac{30}{f_c} \right)^{1/3} \right] \right\} \quad \text{Eq. (3-8)}$$

Following Gerges *et al.* (2015), the tensile strength of the cold joint  $f_{ct,j}$  can be computed as follows:

$$f_{ct,j} = 0.25 \sqrt{f_c} \quad \text{Eq. (3-9)}$$

The slip corresponding to ultimate dowel action force is  $0.10d_b$  -  $0.20d_b$ , where  $d_b$  is bar diameter (Randl 2013).  $0.15d_b$  is adopted in this study.

The tangential stiffness of the interface material is assumed to be the ratio of shear strength with dowel action to the slip at maximum dowel action ( $\tau_r/0.15d_b$ ). The nominal stiffness is assumed to be ratio of concrete compressive strength  $f_c$  to displacement at peak strength, which is 0.2 mm according to Duran *et al.* (2017). No softening is assumed in the shear strength  $\tau_r$ , which is defined as cohesion factor in the software. However, a linear tension softening function is assumed with tension stiffening at 40% of the tensile strength  $f_{ct,j}$ .

Table 3.3. Summary of cold joint parameters.

Shear Strength with Dowel Action, $\tau_r$ [MPa]	Eq. (3-7) (fib 2010)
Tensile Strength, $f_{ct,j}$ [MPa]	$0.25\sqrt{f_c}$ (Gerges et al. 2015)
Coefficient of Friction, $\mu_c$	0.6 (fib 2010)
Surface Roughness	Smooth
Slip at Maximum Dowel Action [mm]	$0.15d_b$ (Randl 2013)
Displacement at ultimate concrete compressive strength, $w_o$ [mm]	Duran <i>et al.</i> (2017)
Tangential Stiffness, $K_t$ [N/mm <sup>3</sup> ]	$\tau_r/0.15d_b$
Nominal Stiffness, $K_n$ [N/mm <sup>3</sup> ]	$f_c/w_o$
Cohesion Softening	N/A
Tension Softening	Linear
Tension Stiffening	$0.40f_{ct}$ (fib 2010)

# 4

## ANALYSIS OF RESULTS

---

This chapter deals with the exhibited performance of RC columns and their numerical assessment. The hysteric responses of the RC columns are first revealed, and then engineering demand parameters of prime interest (e.g., initial stiffness, stiffness degradation, energy dissipation, displacement ductility etc.) are computed. The comparison of current experimental results with the FE solution and its effectiveness are summarized as well. Refined numerical models are investigated in detail to identify the factors affecting the overall response.

### 4.1 Hysteric Response

#### 4.1.1 As-Built Specimens

The specimen E1-T-H, which has continuous longitudinal reinforcement from the foundation to the column tip and axial load ratio  $\sigma_N$  of 0.32, could not sustain the load until subsequent drift levels. The reinforcement yielding was detected at 1.08a% drift ratio by the strain gauges. The corresponding flexural capacity for section yielding was computed as 64.5 kN from section analysis where E1-T-H almost reached that value with the global yielding of the column (i.e., 60.02 kN absolute maximum capacity recorded in the test). The strength deterioration started after 1.51b% drift ratio, which later evolved to a rapid decrease. The first crack in the column-foundation interface occurred at 0.55a% drift ratio, while the first flexural cracks (having about 0.35 mm width) initiated at 1.08b% drift ratio at two different locations. Those were about 180 mm and 340 mm far from the column base. In 1.51a% drift ratio, another flexural crack formed

(having about 0.35 mm width at about 500 mm) while existing cracks were opened (i.e., 1.0 mm). In the subsequent drifts (e.g., 2.11b%), the flexural crack at 180 mm widened to 3 mm with concrete spalling. The severe damage, with a crack width of 6 mm and concrete spalling at several locations, was observed at 2.95a%. The recognizable reinforcement buckling occurred 3.85a% drift ratio. The generated numerical models closely estimated the secant stiffness. The ultimate capacity, post-peak response, and distinct strength loss were reproduced with satisfactory accuracy (Fig. 4.1a). The depth and length of the failure zone were very similar in the numerical and experimental observations (Fig. 4.2a).

The specimen with a conforming lap splice detail and an axial load ratio  $\sigma_N$  of 0.32 (i.e., E1-C-H) could not sustain the lateral load until subsequent drift levels. The monitored absolute maximum column shear was 59.35 kN, while the corresponding column shear for section yielding was obtained as 64.7 kN from section analysis. The global yielding of the column reinforcement was detected at 1.51a% by the strain gauges. The strength started to deteriorate after 1.51b% drift ratio. The rapid strength decrease took place at 2.11a% drift ratio (Fig. 4.1b). The first column-foundation interface crack occurred at a drift ratio of 0.39a% while visible flexural cracks initiated at 1.51a% drift ratio (Fig. 4.2b). Later, severe cracks were followed by concrete crushing at about 180 mm from the column base. The slight buckling of column reinforcement was observed at the end of the test. The numerical model accurately reproduced the overall crack pattern and failure mode. The response parameters, such as secant stiffness, ultimate lateral load capacity, and strength deterioration, were closely estimated by the refined models.

The non-conforming hook detail with a high axial load ratio was represented by E1-NC-H specimen. The column shear corresponding to the sectional yielding was computed as 65.3 kN from the section analysis. The absolute maximum column shear, which was monitored in the test, was 58.15 kN. This discrepancy could be due to high slip demand. The strain gauge in the column reinforcement captured the yielding of the reinforcement at 1.51a% drift ratio. Note that the length of the lap splice, which is  $50d_b=700$  mm, was enough to develop reinforcement yielding even though there was no hook at the end of the reinforcements. Like other specimens, the strength degradation was started at a 2.11a% drift ratio (Fig. 4.1c). The first crack at the column-foundation interface occurred at 0.39a% drift ratio. The flexural cracks in the hairline form occurred at 1.51a%. The significant interface opening due to slip of the reinforcement and concrete crushing took place in the subsequent drift levels. The reinforcement slightly buckled

at the end of the test (Fig. 4.2c). The numerical model was capable of reproducing the overall failure mode together with the cyclic response. Due to the significant slip of the reinforcement bar, the pinching response in the subsequent drift ratios was not accurately captured by the numerical model, even though the model considers the bond-slip behavior.

The specimen E1-T-L with low axial load ratio (i.e.,  $\sigma_N=0.15$ ) and continuous longitudinal reinforcement from the foundation to the column tip exhibited slightly better ductile performance than E1-T-H (i.e., equivalent in reinforcement scheme but high axial load). The absolute maximum column shear recorded during the test was 40.04 kN. The sectional yield capacity of the specimen in terms of column shear was computed as 43.5 kN from the section analysis. The yielding of the column reinforcement, measured by the strain gauges, was at 1.08a% drift ratio. The strength degradation was not as distinct as the one with a high axial load, which resulted in higher ductility. The contribution of the axial load on the bond-slip response revealed itself as a pinching effect. The relatively wider loops in the case of E1-T-H (Fig. 4.1a) were not observed in E1-T-L (Fig. 4.1d). The first crack as an interface opening initiated at 0.28a% drift ratio. The first flexural cracks in hairline form (i.e., crack width of 0.20 mm) formed at about 120 and 260 mm from the column base. The cracks did not distribute along the plastic hinge length, forming a few with large crack widths. The partial concrete spalling took place at 2.95a% drift ratio, which evolved to slight reinforcement buckling in the subsequent drift level (Fig. 4.2d). The numerical model captured the all response quantities with sufficient accuracy.

The specimen E1-C-L was constructed with conforming hook detail and tested under a low axial load ratio. The absolute maximum column shear was monitored as 38.46 kN. On the other hand, the column shear corresponding to sectional yielding was computed as 43.8 kN. The strain gauges measured the yielding of the reinforcement at 1.08a% drift ratio. Compared to a specimen with an identical reinforcement scheme but a high axial load (e.g., E1-C-H), the strength deterioration was less recognizable, which shows the adverse effect of high axial load on the flexural behavior of the columns. Narrower loops compared to E1-T-L (i.e., continuous longitudinal reinforcement with low axial load) were monitored in hysteric response. It is, therefore, concluded that the bond-slip response was more prominent in the case of E1-C-L. No significant flexural cracks in the place of potential plastic hinge length were observed, while the interface crack at the column foundation connection took place at 0.28b% drift ratio. Due to the low axial load ratio, the interface cracks formed earlier than the one with an identical

reinforcement scheme but a high axial load (i.e., E1-T-H). The partial concrete spalling took place at 2.95a% drift ratio while no significant reinforcement buckling was observed. The numerical model closely estimated the secant stiffness, ultimate load, overall hysteric response (Fig. 4.1e), and failure mode (Fig. 4.2e). However, the numerical model did not fully capture the pinching effect in the subsequent cycles. It is due to implemented bond-slip model, which accounts semi-circle phenomenon with limited aspects (see Section 3.2.3).

E1-NC-L represented the non-conforming hook detail with a low axial load ratio. The column shear corresponding sectional yielding was computed as 43.8 kN from the section analysis. The monitored absolute maximum column shear in the test was 35.38 kN. The discrepancy in the results arises from the significant slip of the reinforcement. The section analysis does not consider the slip degradations. The lowest capacity in the low axial load specimens' group was observed in E1-NC-L. The strain gauges measured the yielding of the reinforcement at 1.08a% drift ratio. Note that the lap-splice distance is sufficient enough to develop a reinforcement yielding even though there was no hook in E1-NC-L. Therefore, the capacity of the specimen with non-conforming hook detail (E1-NC-L) and the specimen with conforming hook detail (E1-C-L) is closely comparable. However, very narrow loops in the hysteric response show the adverse effect of significant slip (Fig. 4.1f), which also decreased the energy dissipation capacity. The formed cracks were not distributed along the potential plastic hinge zone (Fig. 4.2f). Those mostly concentrated on the column-foundation interface. A single interface crack also resulted in a low energy dissipation. The first interface crack occurred in the early stage of the loading regime. The partial concrete spalling in the concrete cover took place in the subsequent drift levels (which is due to low-strength concrete), while no significant reinforcement buckling was monitored. The numerical model could accurately reproduce the response quantities such as secant stiffness, ultimate capacity, and strength deterioration. However, the pinching effect was not captured well in the subsequent drift levels due to limited features of the semi-circle phenomenon implemented bond-slip model.

Table 4.1. Summary of measured damage quantities.

First Damage	E1-T-H	E1-C-H	E1-NC-H	E1-T-L	E1-C-L	E1-NC-L
Column-Foundation Interface Crack	0.55a%	0.39a%	0.39a%	0.28a%	0.28b%	0.28a%
Flexural Crack	1.08b% (0.35 mm at about 180 mm and 340 mm from column base)	1.51a% (0.35 mm at about 350 mm, 0.15 mm at about 480 mm)	1.51a% (0.15 mm at about 350 mm, 0.10 mm at about 240 mm)	0.77a% (0.20 mm at about 120 mm and 260 mm)	0.77a% (0.20 mm at about 110 mm and 255 mm)	0.77a% (0.20 mm at about 125 mm and 260 mm)
Shear Crack	--	--	--	--	--	--
Concrete Spalling	2.11a% (at about 200 mm)	1.08a% (partial spalling closer to column-foundation interface)	2.11a% (at about 180 mm in concrete cover)	2.95b% (partial spalling in the concrete cover)	2.95b% (partial spalling in the concrete cover)	2.95a% (partial spalling in the concrete cover)
Reinforcement Yielding	1.08a%	1.51a%	1.51a%	1.08a%	1.08a%	1.08a%
Reinforcement Buckling	3.85a%	3.85a%	3.85a%	3.85a%	--	--
State at the end of the test	Concrete crushing with reinforcement buckling, heavy damage at about 240 mm from the column base	Concrete crushing with slight reinforcement buckling and interface opening about 8 mm	Concrete crushing with slight reinforcement buckling and interface opening about 12 mm	Concrete crushing with reinforcement buckling and heavy damage at about 240 mm from the column base	Local concrete crushing near interface and interface opening about 15 mm	Local concrete crushing near interface and interface opening about 18 mm

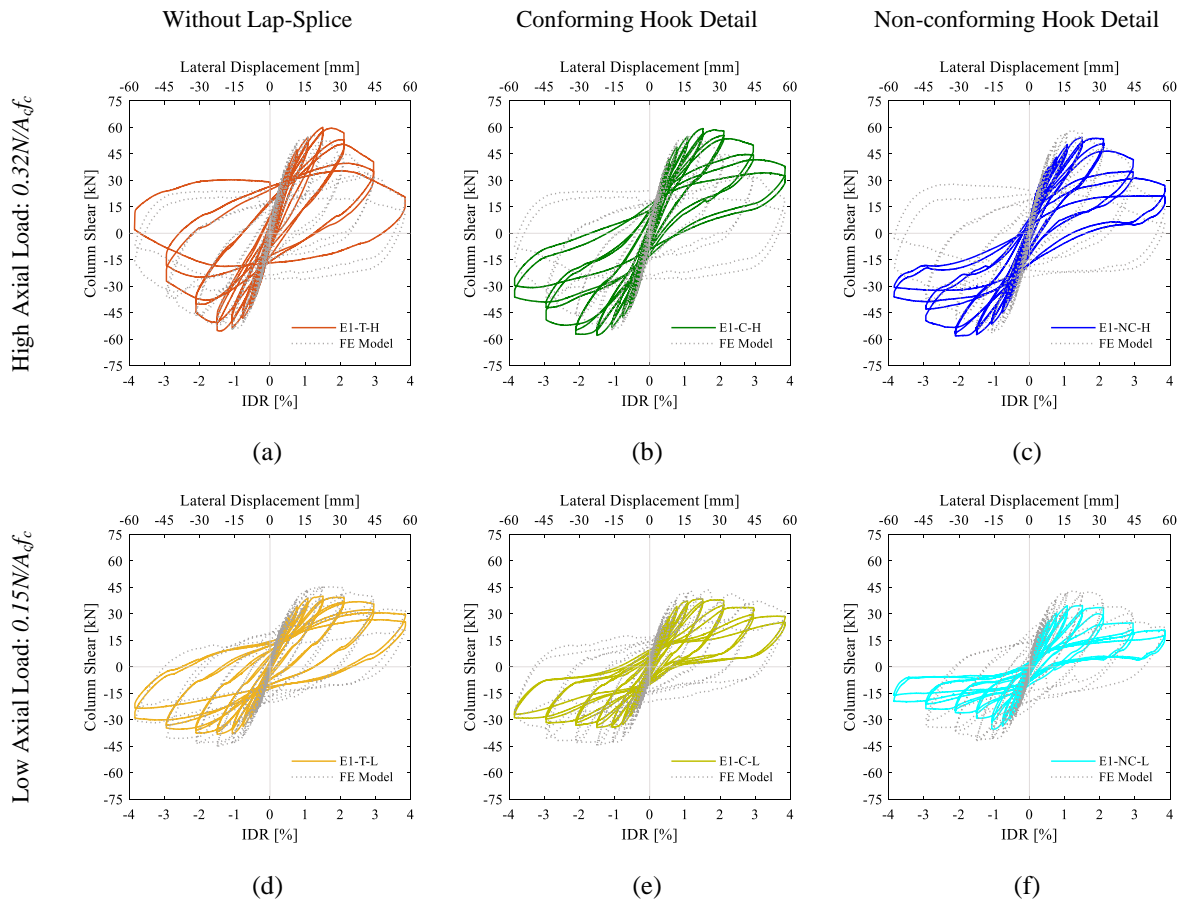


Fig. 4.1. Hysteric response of as-built specimens (a) E1-T-H (b) E1-C-H (c) E1-NC-H (d) E1-T-L (e) E1-C-L (f) E1-NC-L.



Fig. 4.2. Damage evaluation in as-built specimens (a) E1-T-H (b) E1-C-H (c) E1-NC-H (d) E1-T-L (e) E1-C-L (f) E1-NC-L.

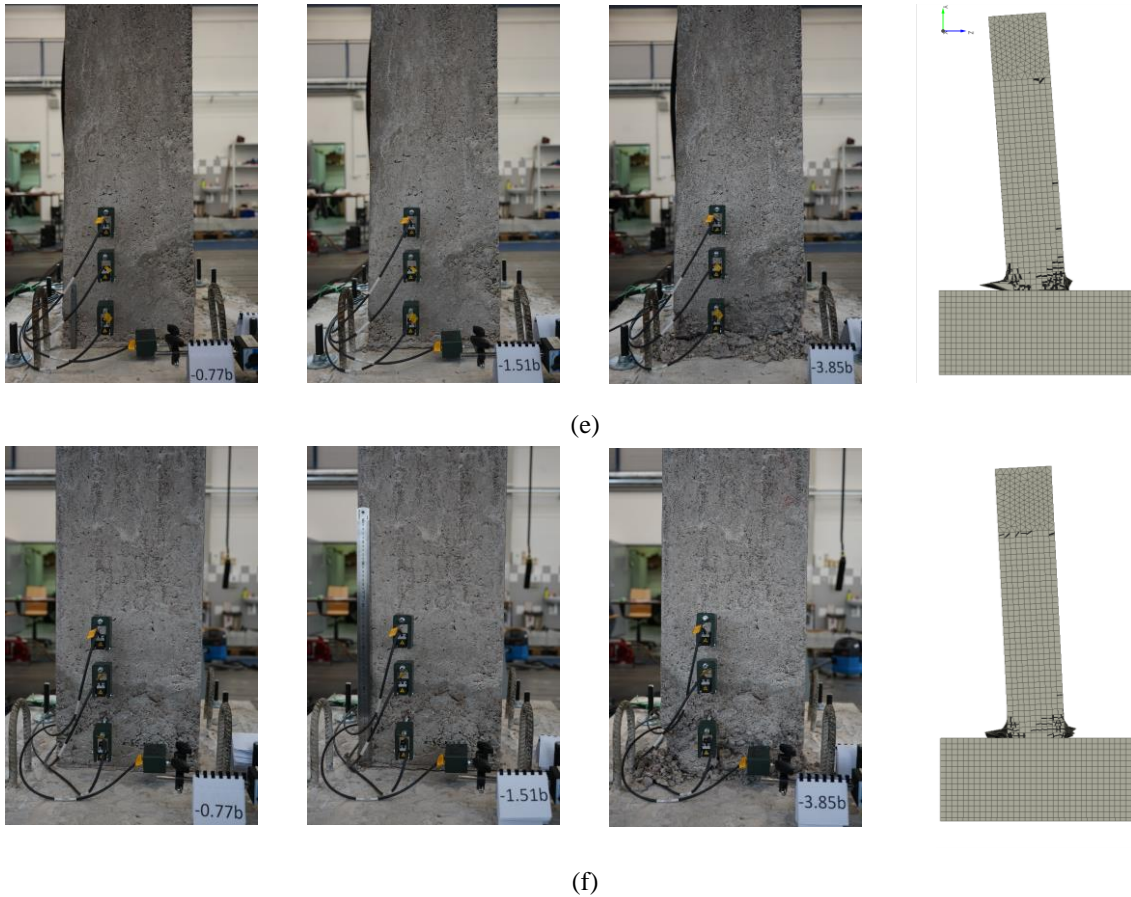


Fig. 4.2 (cont.). Damage evaluation in as-built specimens (a) E1-T-H (b) E1-C-H (c) E1-NC-H (d) E1-T-L (e) E1-C-L (f) E1-NC-L.

### 4.1.2 Repaired Specimens

The first structural repair test was conducted on specimen E1-T-H (i.e., a specimen with high axial load and continuous longitudinal reinforcement from the foundation to the column tip), becoming specimen E1-T-H-R. The as-built form of the specimen (E1-T-H) developed very severe cracks in the order of centimeters at the column base and concrete crusting with reinforcement buckling. In the repair attempt, such effects were minimized by the contribution of the longitudinal and transverse CFRPs. The lateral load capacity of the as-built specimen was recovered by the repaired scheme. Unlike the as-built case, the repaired specimen exhibited a gradually deteriorating load capacity (Fig. 4.3a). Of course, this stepwise failure increased the displacement ductility demand up to a certain level. However, the formation of the visual damages, such as the debonding or local fracture of CFRP, was an inevitable failure in the subsequent drift level (Fig. 4.4a).

The repaired form of E1-C-H (i.e., a specimen with high axial load and conforming hook detail in the lap splice) yielded the specimen entitled E1-C-H-R after repair. The lateral strength was

recovered and even significantly enhanced from its as-built form. The strength deterioration was not distinct (Fig. 4.3b). The secant stiffness and stiffness degradation provided by the proposed repairing method were sufficient enough as well. The contribution of the proposed repaired scheme to the enhancement of bond-slip response was limited as narrower loops were observed. There was no significant debonding or tearing of the CFRP sheets, except the stress concentration zones in the subsequent drift levels (Fig. 4.4b). This clearly proves the effectiveness of the proposed structural repair.

The third repair test was conducted on the specimen with high axial load and non-conforming hook detail, yielding E1-NC-H-R. The repair attempt showed that the lateral load capacity and other response parameters of prime interest could be partially (or fully) recovered even when deep interface cracks or concrete crushing were developed (Fig. 4.3c). The longitudinal-CFRP debonding was observed in 1.51a% drift ratio level, which evolved to CFRP fracture in the following drift level. Additional stresses developed in the transverse CFRP due to CFRP fracture's debonding, followed by CFRP tearing in the transverse direction (Fig. 4.4c). The CFRP failure was very sudden and took place in the first phase of the last loading cycle (i.e., 3.85a%).

The fourth structural repair test was conducted on the specimen with low axial load and continuous longitudinal reinforcement from the foundation to the column tip (i.e., E1-T-L), becoming the specimen E1-T-L-R. The axial failure in the as-built configuration was transformed to a flexural kind of failure mode, confirming that the repair attempt contributes to the overall performance of the column. The repaired scheme fully recovered the lateral load capacity of the as-built specimen without any gradual or distinct deterioration in the lateral load capacity (Fig. 4.3d). This ensured a certain displacement ductility level. As the displacement increases, the flexural behavior was accompanied by more micro damages, such as the local debonding or fracture of CFRP (Fig. 4.4d). Conversely, this did not remarkably affect the overall response.

The repaired form of E1-C-L (i.e., a specimen with low axial load and conforming hook detail in the lap splice) becomes E1-C-L-R. Compared to one with similar hook detail but low axial load, the adverse effect of the axial load was not revealed in this specimen. The large interface opening in the as-built configuration was transformed into a flexural failure mode. The repair attempt enhanced the overall performance of the column. No gradual or distinct deterioration in the lateral load capacity was monitored (Fig. 4.3e). Therefore, an enhancement in

displacement ductility was also achieved. On the other hand, the repair attempt did not contribute to the improvement of the bond-slip response, resulting in narrower loops in cyclic response. Except for local micro damages in the CFRP, no visual failure occurred (Fig. 4.4e).

The repaired form of the specimen with low axial load and nonconforming hook detail became E1-NC-L-R. The lateral load capacity of the as-built form was recovered at a certain level. Like all other repaired specimens with low axial load, the displacement ductility enhanced significantly. The repaired specimen sustained the lateral load capacity until the last loading cycle (Fig. 4.3f). The repair attempt enhanced the flexural behavior, while CFRP did not remarkably contribute to the bond-slip response. Therefore, the pinching effect was not improved, resulting in narrower loops in the cyclic response. The visual damage in the form of local debonding or fracture in the stress-concentrated places was mainly at a micro level (Fig. 4.4f), which did not affect the overall response.

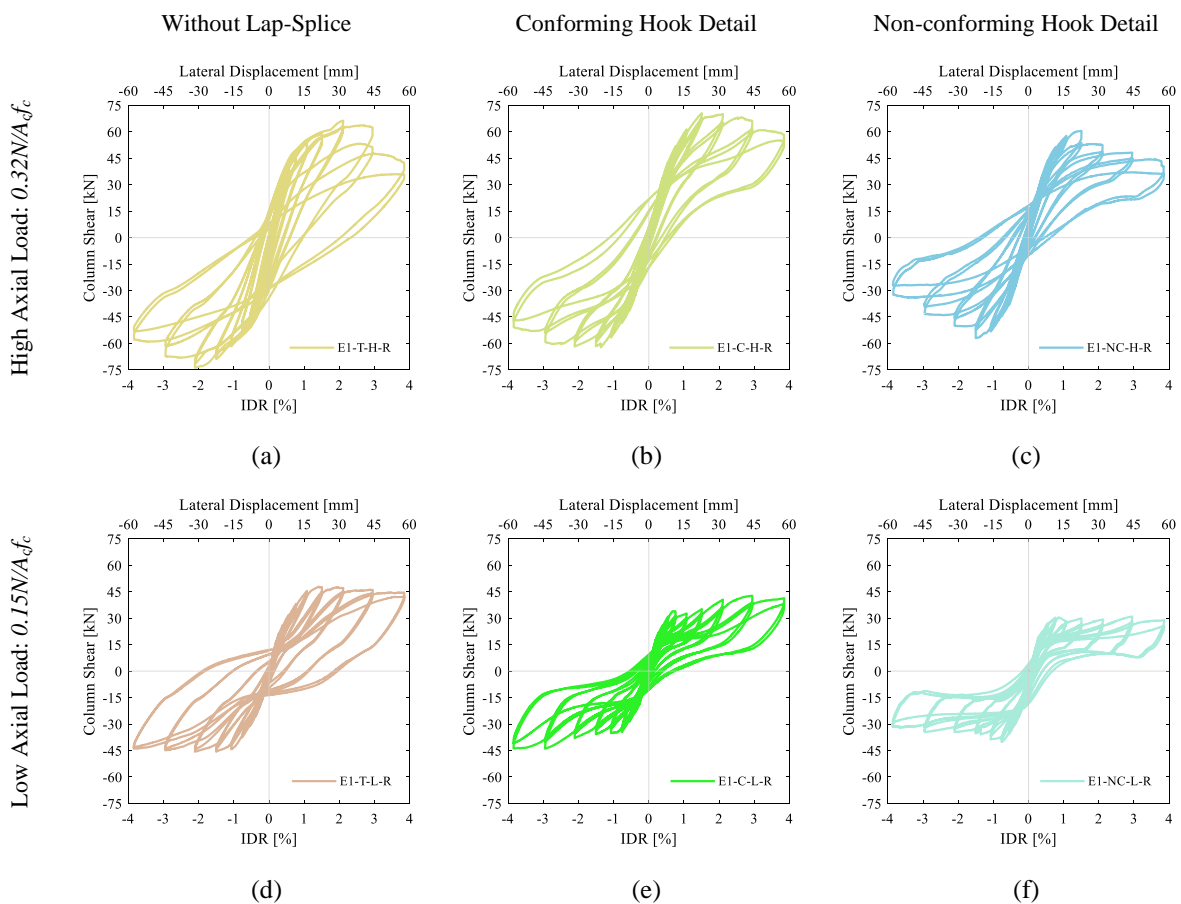


Fig. 4.3. Hysteric response of repaired specimens (a) E1-T-H-R (b) E1-C-H-R (c) E1-NC-H-R (d) E1-T-L-R (e) E1-C-L-R. (f) E1-NC-L-R.

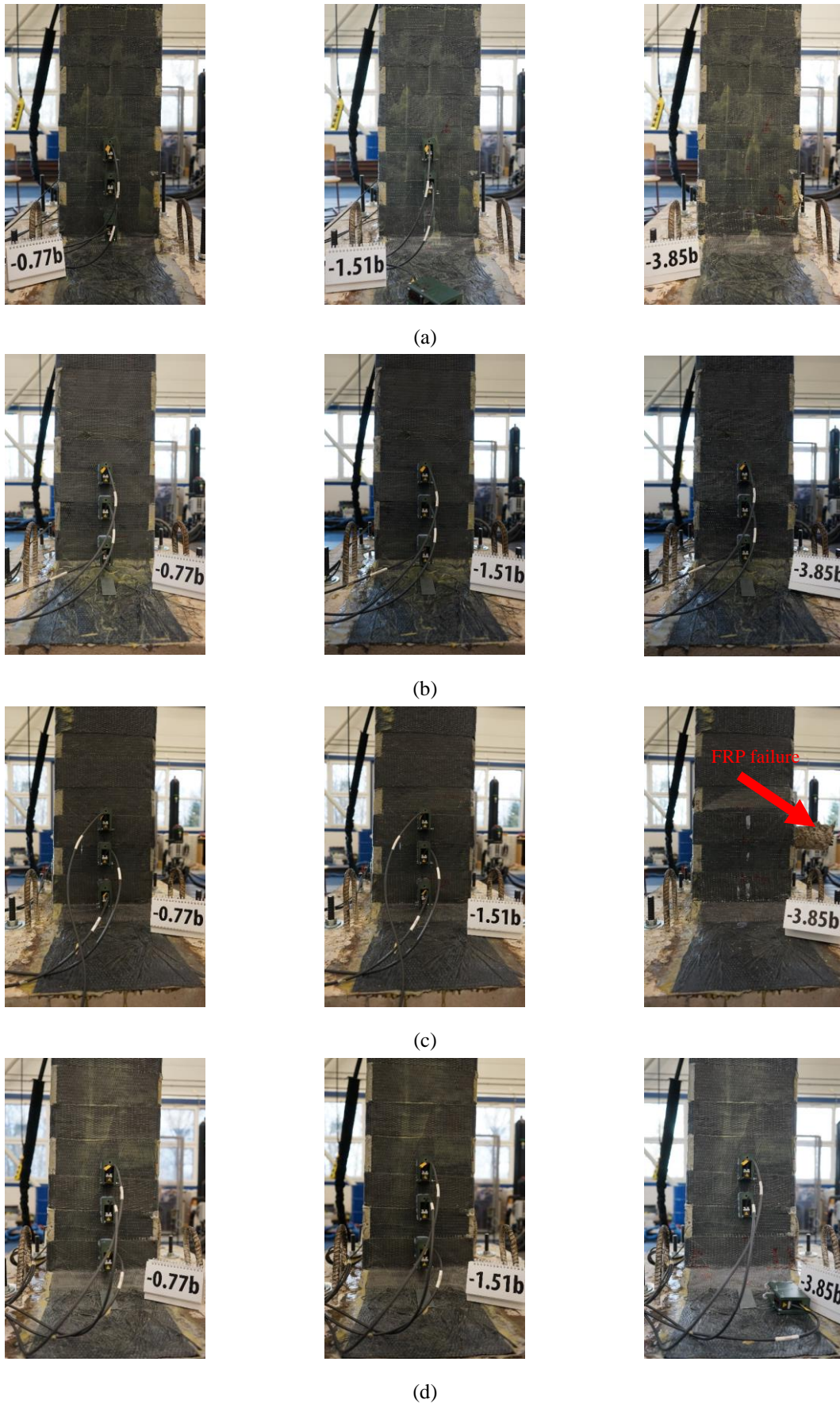


Fig. 4.4. Damage evaluation in repaired specimens (a) E1-T-H-R (b) E1-C-H-R (c) E1-NC-H-R (d) E1-T-L-R (e) E1-C-L-R. (f) E1-NC-L-R.

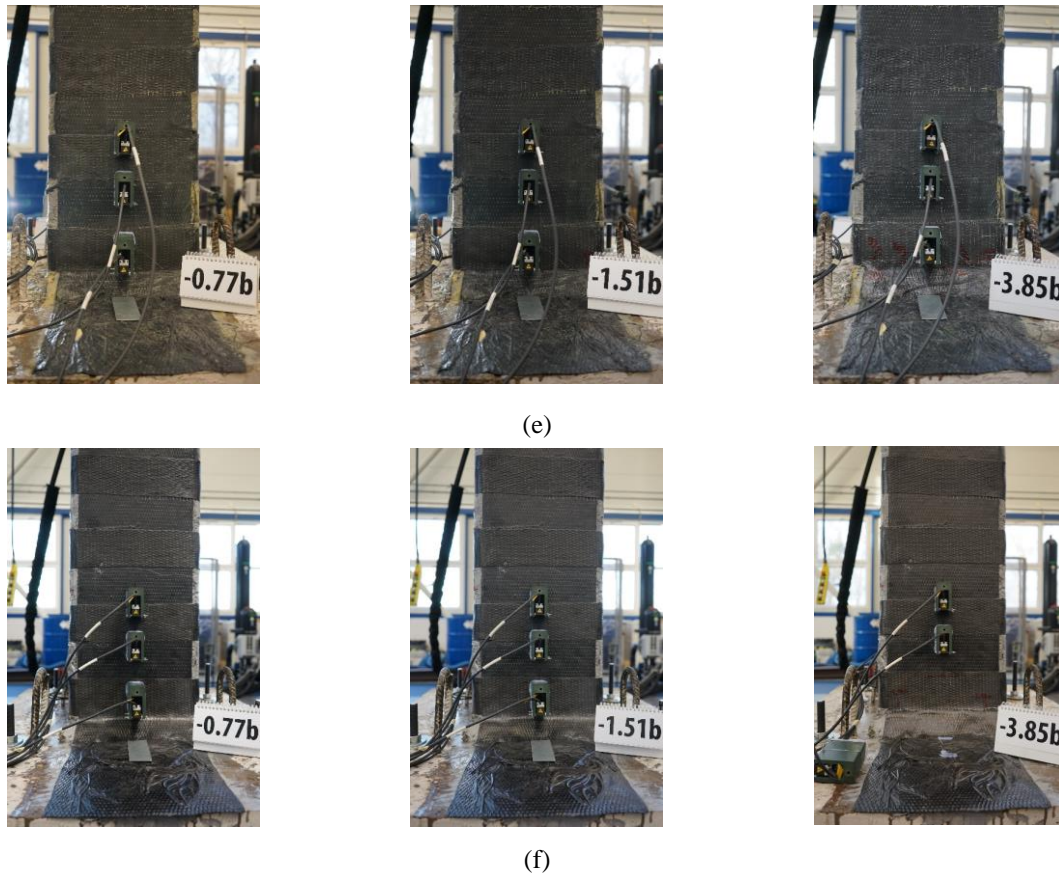


Fig. 4.4 (cont.). Damage evaluation in repaired specimens (a) E1-T-H-R (b) E1-C-H-R (c) E1-NC-H-R (d) E1-T-L-R (e) E1-C-L-R. (f) E1-NC-L-R.

## 4.2 Engineering Demand Parameters

### 4.2.1 Strength

The strength parameters are discussed in terms of column shear  $V_c$ . The capacity of the specimens was recovered by the implemented repair solution. The recorded column shear  $V_c$  in the repaired specimens was higher in the inelastic part of the hysteric response in many cases. For the repaired specimens with low axial load (Fig. 4.5d-f), the strength drop was not as noticeable as in the case of as-built specimens. The repaired specimens with low axial load could sustain the ultimate lateral load even in the latter cycles. In turn, the adverse effect of high axial load actuated FRP debonding in preceding cycles (Fig. 4.5a-c). Nevertheless, the repaired specimens exhibited a gradually deteriorating load capacity. This stepwise failure, of course, increased the displacement ductility demand up to a certain level. The pinching response was not enhanced significantly. The bond-slip response still dominated the overall response, even in the repaired specimens.

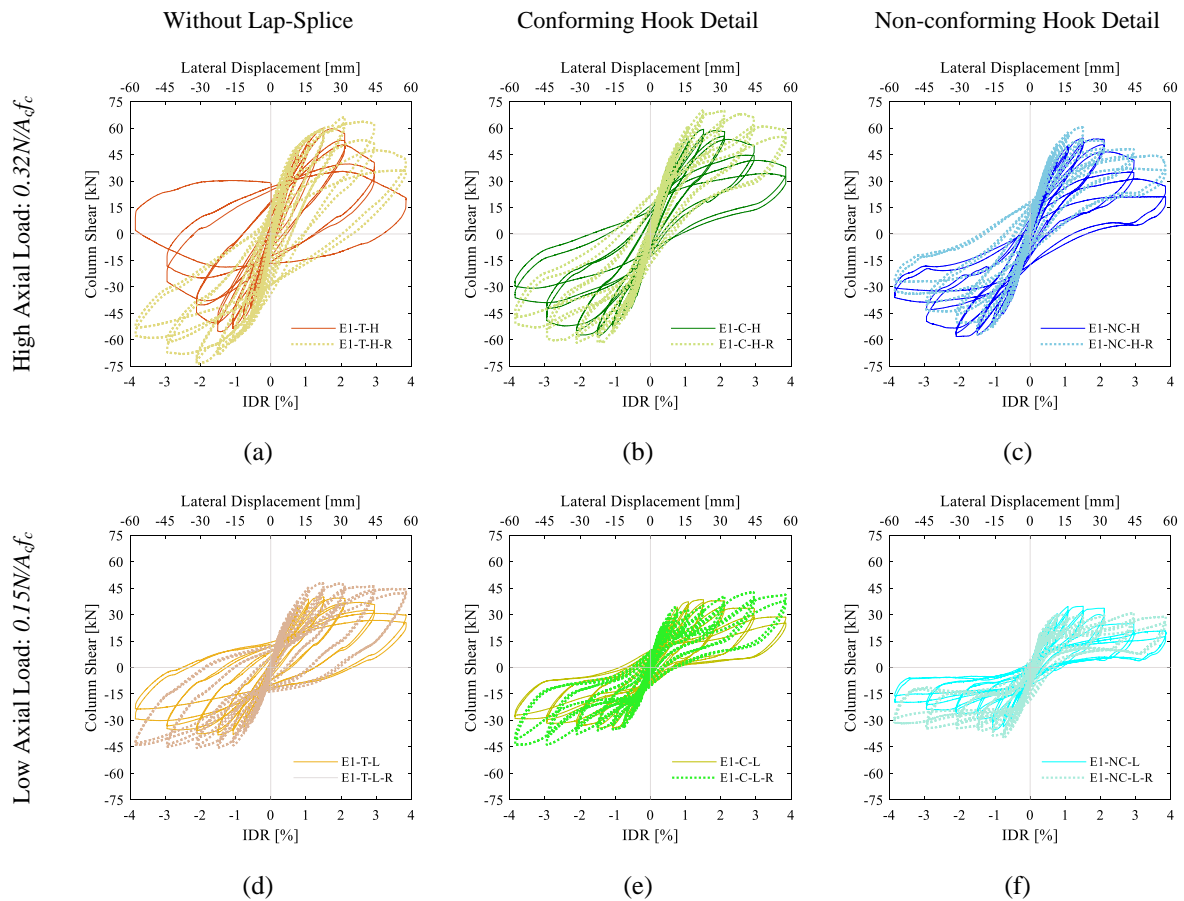


Fig. 4.5. Comparison of hysteretic responses specimen with (a) high axial load and no lap-splice (b) high axial load and conforming hook (c) high axial load and non-conforming hook (d) low axial load and no lap-splice (e) low axial load and conforming hook (f) low axial load and non-conforming hook.

The nonlinear backbone curves of all specimens were obtained from cyclic responses (Fig. 4.6a and b). The relative effect of the repair scheme on the strength was visible on the envelope curves. The column shear capacity was not only recovered by the implemented repair scheme, but also the distinct strength loss was less pronounced in the repaired specimens. The findings reflect the relative effect of the axial load ratio in the repair scheme. Increasing the axial load ratio resulted in a more distinct deterioration in the strength.

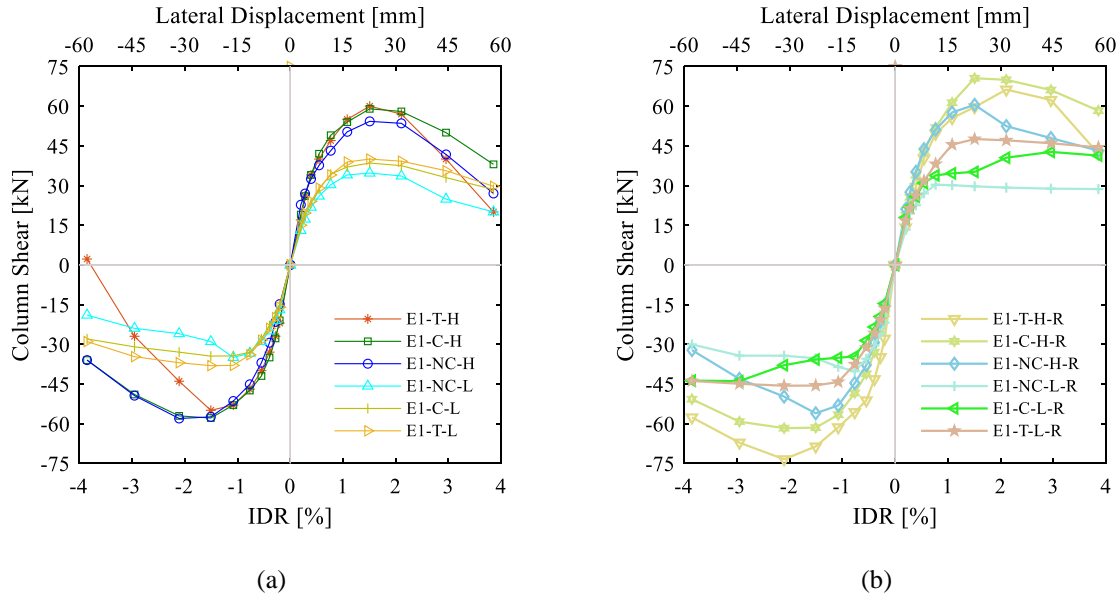


Fig. 4.6. Backbone curves of hysteretic response (a) as-built specimens (b) repaired specimens.

#### 4.2.2 Secant Stiffness and Displacement Ductility

The secant stiffness  $K$  is defined as the slope of the line that joins the origin of the backbone curve and the point where 60% of the ultimate strength is on the ascending part of the envelope curve. Even though the as-built specimens suffer from severe damage [which could possible decrease the secant stiffness], the secant stiffness is restored by the taken repair action (Table 4.2).

The ultimate IDR  $\delta_u$  is taken at 20% strength loss. The drift at effective yielding  $\delta_y$  is computed considering an equivalent elastic-perfectly plastic force-drift relationship obtained from the experimental backbone curve by equating the area under the curves (dissipated energy) (Park 1989). The ultimate IDR  $\delta_u$  and IDR at effective yielding  $\delta_y$  are closely comparable for as-built and repaired specimens (Table 4.2).

The displacement ductility  $\mu_d$  of the subassembly was computed as the ratio of ultimate IDR  $\delta_u$  (taken at 20% strength loss) to the IDR at effective yielding  $\delta_y$ . The repaired specimen could restore the displacement ductility  $\mu_d$ , which can sustain the same demand as per as-built specimens. The test results were further classified according to the achieved displacement ductility  $\mu_d$ . Ductility classes available in the literature (Priestley and Calvi 1991; CEN 2004b; ASCE SEI 41 2017) were considered to group RC columns with similar ductility. This study used the classification concept proposed by ASCE SEI 41 (2017). Accordingly, when displacement ductility  $\mu_d$  is less than 2, it is classified as a low ductile subassembly. Those with displacement ductility  $\mu_d$  ranging between 2 and 4 are considered within the medium ductility

group. When the displacement ductility  $\mu_d$  is greater than 4, RC columns are classified as highly ductile (Table 4.2).

Table 4.2. Summary of engineering demand parameters.

Specimen	Loading Direction	Column Shear, $V_c$ [kN]	Secant Stiffness, $K$ [kN/mm]	Yield Properties			Displacement Ductility, $\mu_d$	$\mu_d$ Class
				Yield Strength, $V_y$ [kN]	Yield IDR, $\delta_y$ [%]	Ultimate IDR, $\delta_u$ [%]		
E1-T-H	+	60.02	5.84	53.95	0.62	2.56	4.14	$\mu_{d,high}$
	-	55.42	5.96	49.40	0.56	2.11	3.78	$\mu_{d,medium}$
E1-C-H	+	59.35	5.83	54.02	0.62	3.16	5.12	$\mu_{d,high}$
	-	57.89	6.22	46.41	0.57	3.14	5.54	$\mu_{d,high}$
E1-NC-H	+	54.37	5.90	49.49	0.56	2.83	5.06	$\mu_{d,high}$
	-	58.15	4.81	50.80	0.74	3.15	4.27	$\mu_{d,high}$
E1-T-L	+	40.04	4.31	36.86	0.57	3.50	6.15	$\mu_{d,high}$
	-	38.27	4.54	31.76	0.52	3.62	6.99	$\mu_{d,high}$
E1-C-L	+	38.46	4.13	35.37	0.57	3.39	5.94	$\mu_{d,high}$
	-	34.46	4.53	28.57	0.47	3.85	8.23	$\mu_{d,high}$
E1-NC-L	+	34.71	3.90	32.19	0.55	2.67	4.85	$\mu_{d,high}$
	-	35.38	5.40	27.42	0.38	1.71	4.47	$\mu_{d,high}$
E1-T-H-R	+	66.29	4.93	60.13	0.81	3.37	4.14	$\mu_{d,high}$
	-	73.77	7.72	62.98	0.57	3.75	6.62	$\mu_{d,high}$
E1-C-H-R	+	70.57	5.45	65.09	0.80	3.85	4.84	$\mu_{d,high}$
	-	62.21	5.48	52.09	0.70	3.85	5.50	$\mu_{d,high}$
E1-NC-H-R	+	60.61	6.17	53.77	0.58	2.87	4.93	$\mu_{d,high}$
	-	56.94	4.94	49.46	0.69	2.73	4.03	$\mu_{d,high}$
E1-T-L-R	+	47.89	4.33	45.51	0.70	3.85	5.50	$\mu_{d,high}$
	-	45.70	4.33	37.74	0.68	3.85	5.65	$\mu_{d,high}$
E1-C-L-R	+	42.73	4.88	38.71	0.53	3.85	7.27	$\mu_{d,high}$
	-	43.97	3.97	38.97	0.66	3.85	5.84	$\mu_{d,high}$
E1-NC-L-R	+	30.95	4.56	28.95	0.43	3.85	9.11	$\mu_{d,high}$
	-	40.21	7.29	31.77	0.32	3.41	10.64	$\mu_{d,high}$

### 4.2.3 Stiffness Degradation

The peak-to-peak stiffness is defined as the slope of the line that connects the ultimate load points in the positive and negative directions of the hysteresis loop in each loading cycle. Evolving to plastic range along with the increased level of damage, a significant decrease in the peak-to-peak stiffness was computed for all specimens. The peak-to-peak stiffness sustained in each loading cycle of as-built specimens was similar to the repaired specimens (Fig. 4.7a and b). The pre-formed cracks in the as-built specimens did not influence the peak-to-peak stiffness in the repaired specimens.

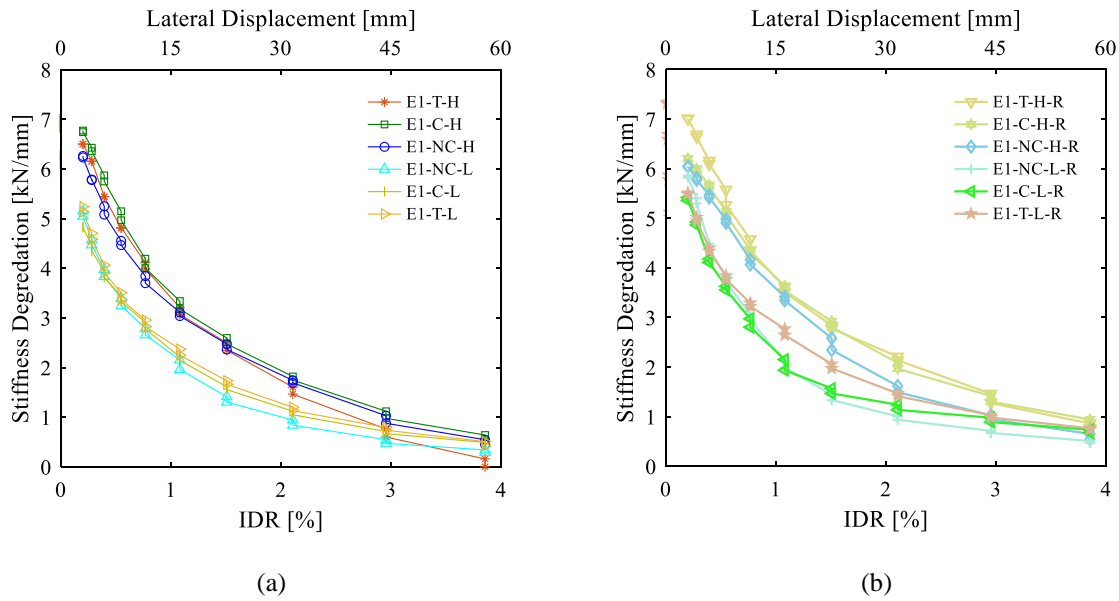


Fig. 4.7. Stiffness degradation (a) as-built specimens (b) repaired specimens.

#### 4.2.4 Dissipated Energy

The enclosed area of each loop in each loading cycle is the dissipated energy  $E_d$  for the corresponding cycle. Then, the sum of areas computed for each loading cycle is the cumulative dissipated energy  $E_d$ . As the overall response of the specimens was governed by significant bond deterioration, the pinching behavior in the hysteric response would not be revealed, which results in low energy dissipation capacity. The high axial load and continuous reinforcement minimized the reinforcement slip, resulting in high dissipated energy (Fig. 4.8a and b). The dissipated energies were closely comparable between as-built and repaired schemes.

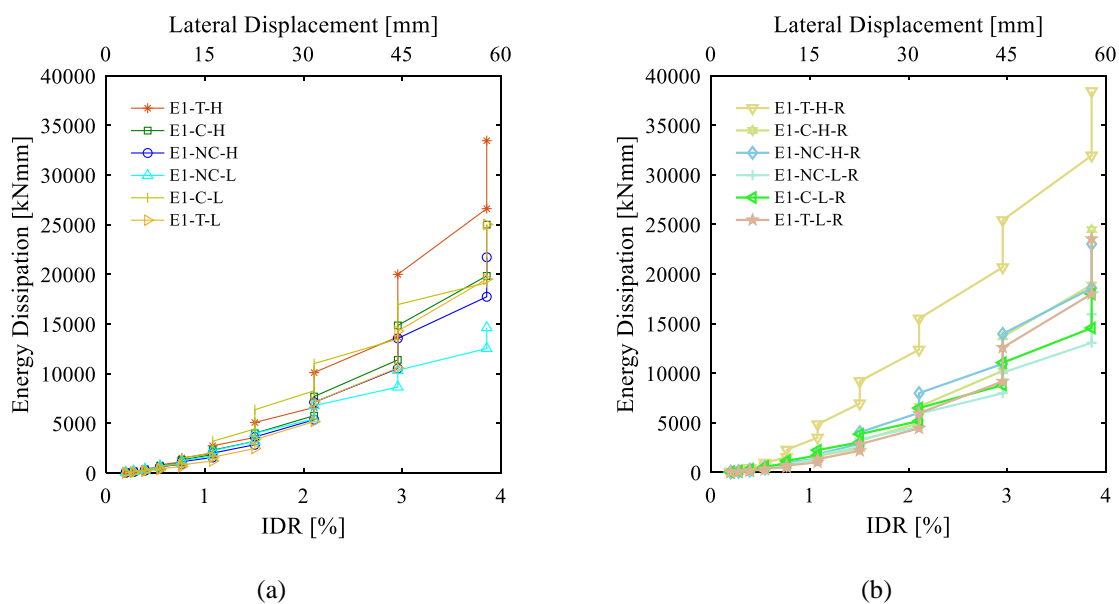


Fig. 4.8. Dissipated energy (a) as-built specimens (b) repaired specimens.

## 4.2.5 Experimental Moment-Curvature Response

The simultaneous measurement of the column base deformation by laser displacement sensors (Fig. 4.9) was used to obtain the curvature at three segments measured from the foundation (i.e., 0-125 mm, 125-260 mm, and 260-370 mm). Following Eq. (4-1), the curvature is obtained while the variables in the formula are visually presented in Fig. 4.9.

$$\phi = \frac{\varepsilon_1 + \varepsilon_2}{L_{ds}} \quad \text{Eq. (4-1)}$$

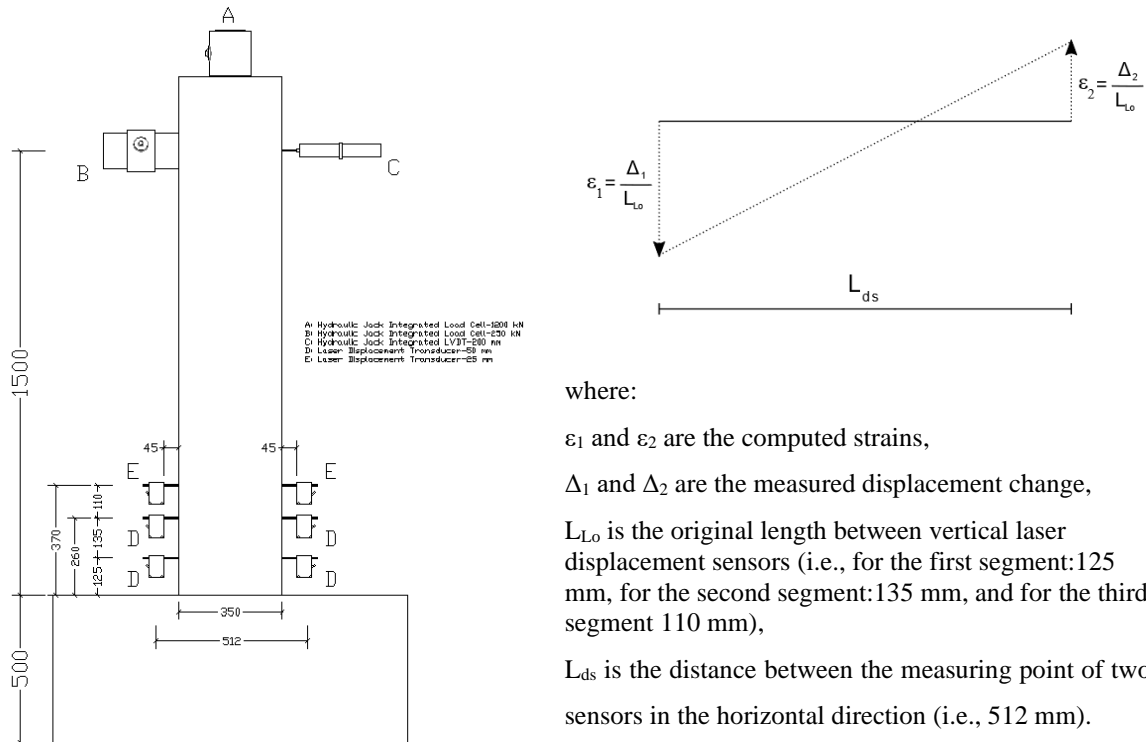
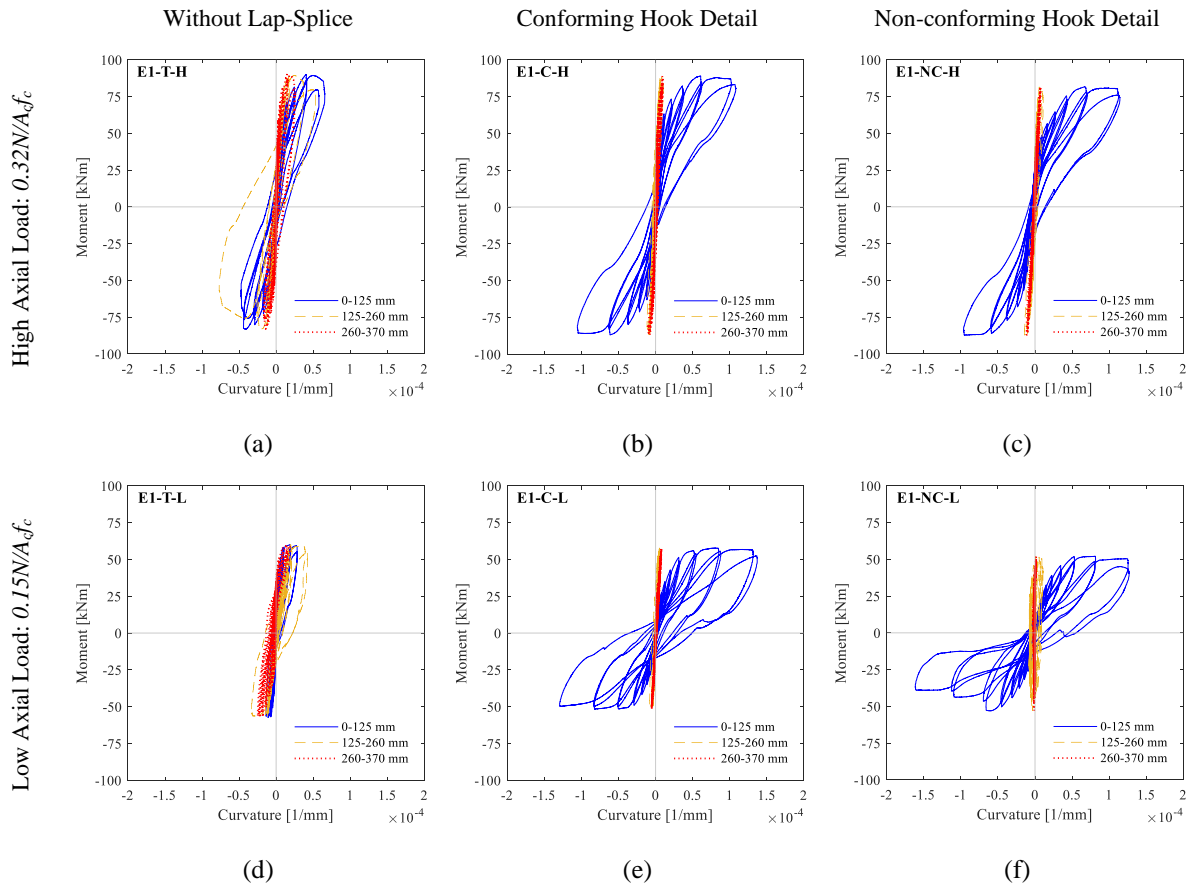


Fig. 4.9. Computation of curvature.

The premature failure of the columns with large cracks in the column-foundation interface and potential plastic hinge zone endangered the laser displacement sensors' stability. Therefore, the computed curvature of the reference specimens was presented up to -2.11b% drift level. The longitudinal reinforcement without lap-splice (i.e., E1-T-H and E1-T-L) allowed the distribution of cracks along the potential plastic hinge zone. Therefore, the curvature demand was distributed between the first (0-125 mm), second segment (125-260 mm), and even third segment (260-370 mm) (Fig. 4.10a and d). The evaluated curvature agreed with the observed failure mode. In the case of the specimen with low axial load and lap splice (i.e., E1-C-L and E1-NC-L), the curvature in the first segment (i.e., 0-125 mm) was the highest (Fig. 4.10c and f). It is due to the significant reinforcement slip in the foundation-to-column interface opening. Increasing axial load (i.e., E1-C-H and E1-NC-H) mitigated the slip demand. Conversely, the

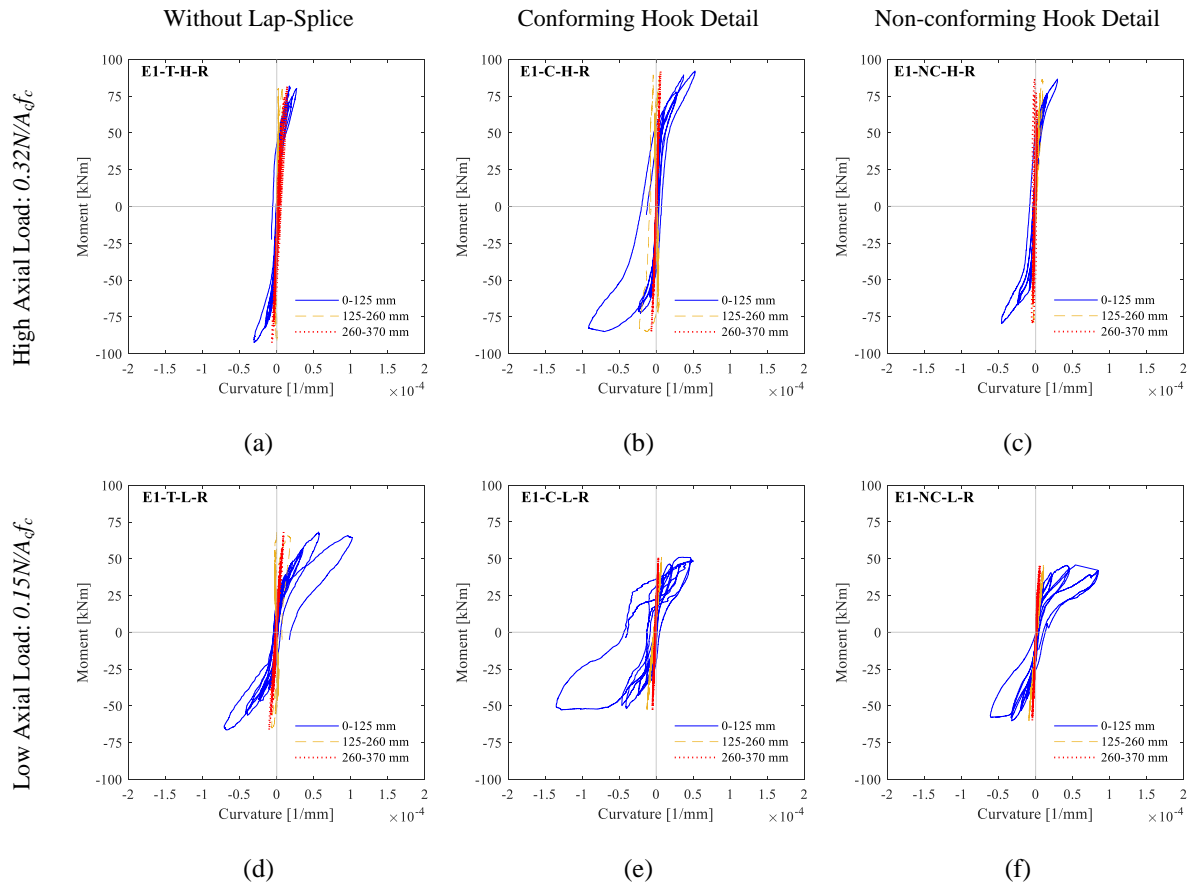
slip in the foundation-to-column interface was the main source of the base rotation (and so curvature) (Fig. 4.10b and e).



Data included up to -2.11b% drift ratio

Fig. 4.10. Experimental moment-curvature relationship of reference specimens (a) E1-T-H (b) E1-C-H (c) E1-NC-H (d) E1-T-L (e) E1-C-L (f) E1-NC-L.

The debonding and local deformations influenced the laser displacement sensors' stability, endangering the measurement reliability. Therefore, the curvature was computed up to -1.08b% drift level in the repaired specimens. Similar to the as-built specimens, the curvature demand was high in the first segment (i.e., column-foundation interface) of the specimens with low axial load (Fig. 4.11d-f). The mitigation of slip demand by the high axial load was in favor of decreasing the curvature demand in the first segment (Fig. 4.11a-c).



Data included up to  $-1.08\%$  drift ratio

Fig. 4.11. Experimental moment-curvature relationship of repaired specimens (a) E1-T-H-R (b) E1-C-H-R (c) E1-NC-H-R (d) E1-T-L-R (e) E1-C-L-R (f) E1-NC-L-R.

## 4.3 Empirical Models

### 4.3.1 Damage Index

The individual engineering demand parameters showed the performance of the RC columns. However, an evaluation, which can combine at most engineering demand parameters, was required. This can be achieved by the probabilistic damage index proposed by Park and Ang (1985). The proposed method combines ultimate displacement  $\Delta_u$ , yield strength  $V_y$ , and dissipated energy  $E_d$ . More information on the calculation of the probabilistic damage index can be found in Del Zoppo *et al.* (2018).

The IDR at the same damage index was higher in the repaired specimens than as-built specimens. The calculated damage index was higher than the as-built specimen, which was compatible with experimental observations (e.g., mitigated damage in the repaired specimens) (Fig. 4.12a and b).

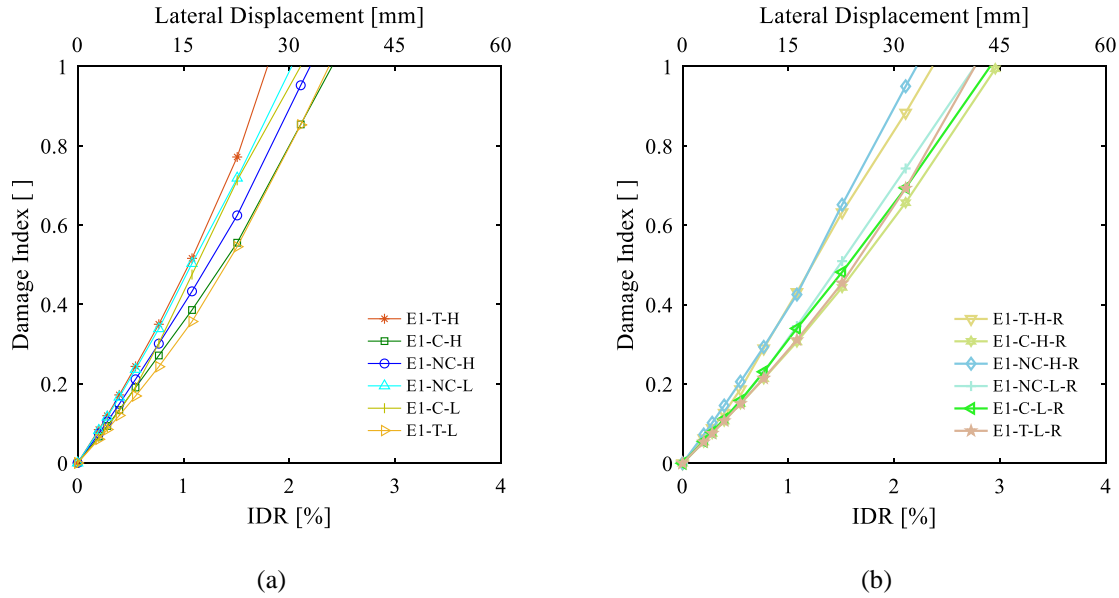


Fig. 4.12. Damage index (a) as-built specimens (b) repaired specimens.

### 4.3.2 Drift at Axial Failure

The model, developed by Elwood and Moehle (2003) to estimate the drift at axial failure for shear-damaged columns, can be adapted to simulate the axial failure of the column. Indeed, the tested specimens did not develop any preceding shear failure. Therefore, the results should be carefully interpreted. On the other hand, the flexural cracks with significant interface opening due to slip significantly deteriorated the specimens capacity (specifically the ones with high axial load), followed by axial failure of the specimens. Eq. (4-2) provides the drift at axial failure.

$$\frac{\delta}{L} = \frac{4}{100} \left[ \frac{1 + (\tan \theta)^2}{\tan \theta + N \left( \frac{s_s}{A_{st} f_{yt} d_c \tan \theta} \right)} \right] \quad \text{Eq. (4-2)}$$

where  $\theta$  is  $65^\circ$ ,  $N$  is axial load,  $s_s$  is spacing between stirrups,  $A_{st}$  is the area of shear reinforcement,  $f_{yt}$  is the yield strength of the shear reinforcement,  $d_c$  is the depth of the column core from the center line to center line of the stirrups,  $\delta$  is the drift,  $L$  is the column height (i.e.,  $\delta/L$  is the IDR). By implementing Eq. (4-2) for the tested specimens, the drift ratio at axial failure was found as 1.81% for specimens with high axial load (i.e., axial load ratio of  $\sigma_N=0.32$ ). That of specimens with low axial load (i.e., axial load ratio of  $\sigma_N=0.15$ ) was obtained as 4.36% (Fig. 4.13a and b). The results were partially compatible with experimental observations. The specimens with high axial load developed an axial failure, while bond degradation was more

prominent for the specimens with low axial load. Therefore, the axial damage level was less for the specimens with low axial load.

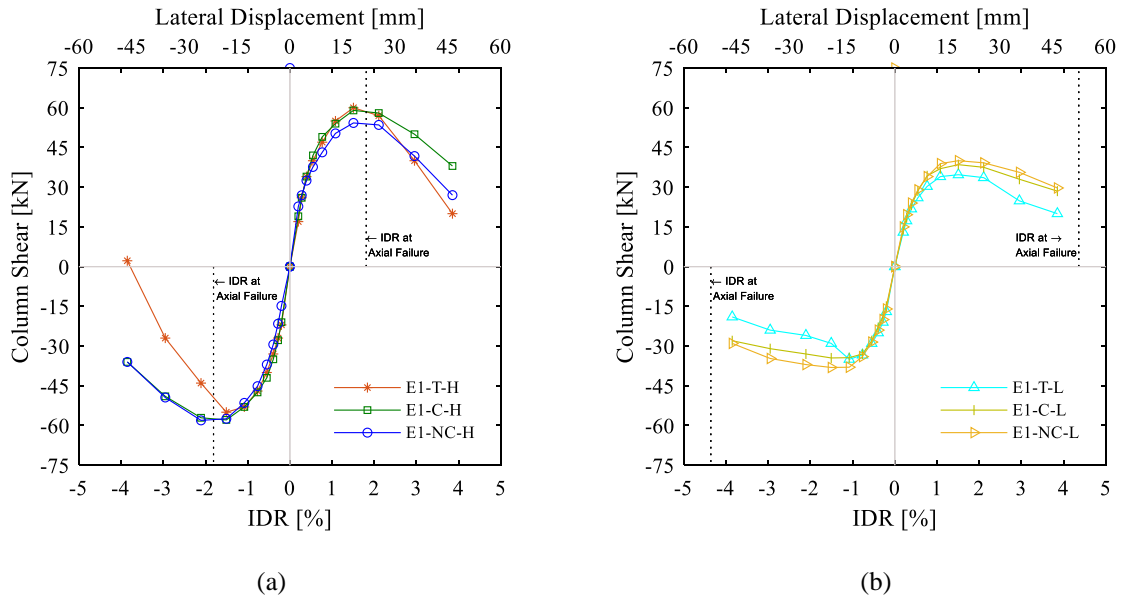


Fig. 4.13. IDR at axial failure (a) as-built specimens with high axial load (b) as-built specimens with low axial load.

### 4.3.3 Backbone Model and Performance Levels

The backbone model proposed in ASCE SEI 41 (2017) is adapted to characterize the cyclic response. The lateral load-plastic rotation angle is defined by three modeling parameters, which are  $a$ ,  $b$ , and  $c$ . Parameter  $a$  defines the plastic rotation angle at the onset of lateral strength loss, parameter  $b$  is the plastic rotation angle measured to the onset of axial failure, and parameter  $c$  is defined as the ratio between the residual lateral strength at axial failure and the peak lateral strength (Hassan and Elmersy 2022). The computed modeling parameters were presented along with the cyclic response of each as-built specimen (Fig. 4.14a-f). Here, the hardening is not considered when constructing the backbone curves. The model overestimates the cyclic response. The model was believed to be calibrated for specimens without significant slip, reducing the ultimate capacity. Besides, the backbone model replicated the failure at axial load lower than experimental response for the specimen with a high axial load. In the case of low axial load, the specimens with less pronounced slip, such as E1-T-L and E1-C-L, the backbone model closely reproduced the hysteric response. That of E1-NC-L overestimated the column shear since the backbone model does not account for slip deterioration.

The ASCE SEI 41 (2017) performance levels (and so modeling parameters) are sensitive to axial load. The Life Safety (LS) performance was lower than the sectional yielding. The gap

between Immediate Occupancy (IO) and Collapse Prevention (CP) limit was relatively high in ASCE SEI 41 (2017) for specimens with a low axial load. The gap was closed for a high axial load specimens. Eurocode 8 (CEN 2005) accumulated the performance level closer to each other (Fig. 4.14a-e). The Damage Limitation (DL) performance level was higher than the point of sectional yielding. Significant Damage (SD) and Near Collapse (NC) levels were closer to DL. For the specimens with high axial load, the equivalent performance levels (i.e., LS-SD and NC-CP) were closer to Eurocode 8 (CEN 2005) and ASCE SEI 41 (2017). However, those for the specimen with low axial load were not the same.

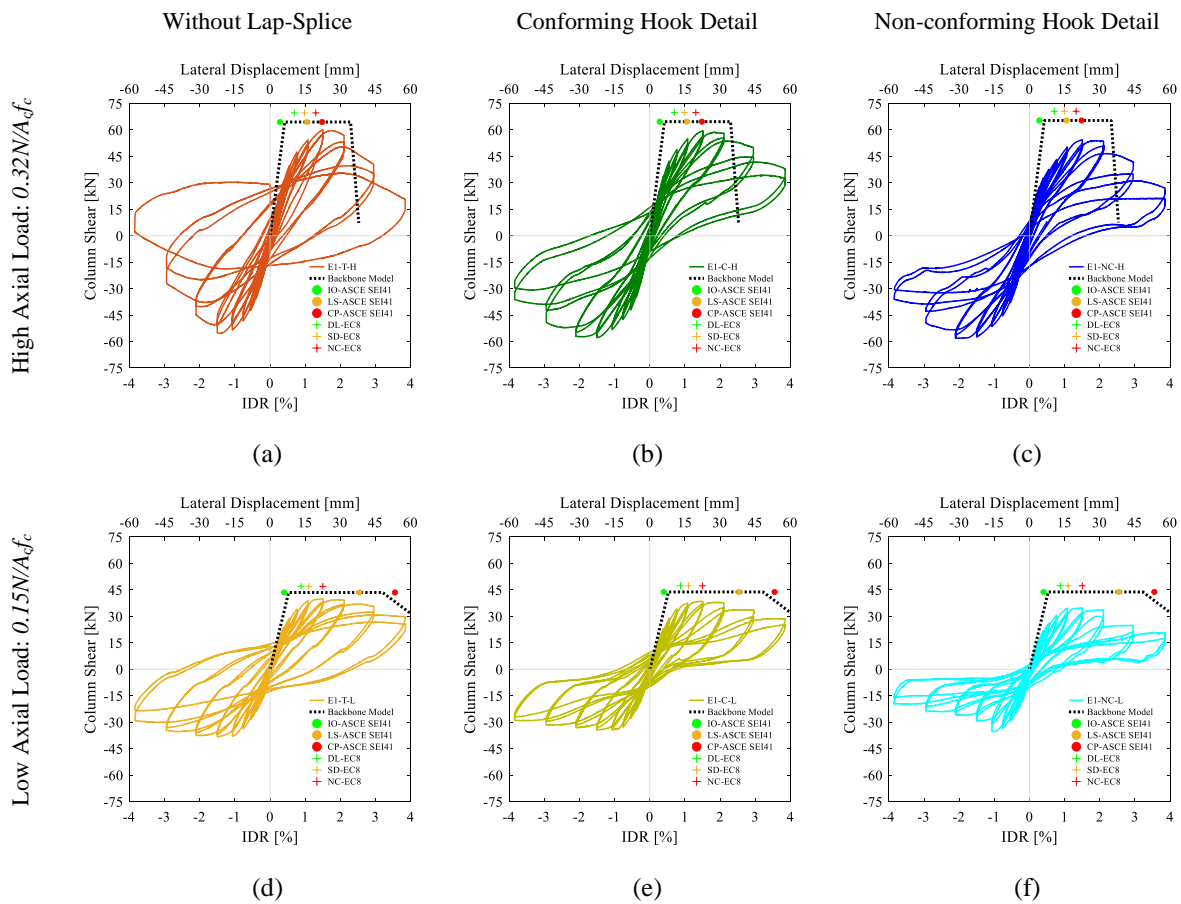


Fig. 4.14. Comparison of ASCE SEI 41 (2017) backbone models with hysteretic responses (a) E1-T-H (b) E1-C-H (c) E1-NC-H (d) E1-T-L (e) E1-C-L (f) E1-NC-L.

# 5

## CONCLUSION

---

### 5.1 Summary

This study investigated the response of substandard RC columns and the repair of the pre-damaged RC columns by experimental and numerical methods. The test variables in 6 specimens were the lap-splice detail and the axial load ratio. The specimens were tested under quasi-static cyclic loading along with the constant axial load. The refined numerical models satisfactorily reproduced all the obtained responses, such as load capacities and crack patterns. After testing the as-built specimens, the specimens suffered from severe damage at the column base. The damaged portion of the RC column was repaired by CFRP sheets, and the tests were repeated. The damage was relocated partially in CFRP. However, the overall capacity and response parameters were recovered.

Based on the study results, the following conclusions were drawn:

- The as-built specimens, analogous to a substandard RC column in current design codes and standards, exhibited poor performance. Being constructed from low-strength concrete with lack of specific details, the specimens were severely damaged. The resulting failure mode was an axial failure with significant slip in all specimens.

- The severity of the damage was high in the specimens with a high axial load ratio (i.e., 0.32). The adverse effect of the high axial load on the damage evaluation was less in the specimens with low axial load (i.e., 0.15).
- Regardless of the hook detail, a lap splice of  $50d_b$  (where  $d_b$  is bar diameter) was enough to reach reinforcement yielding. However, the slip of the reinforcement was more pronounced in the specimens without hooks at the end of the bars. Those also influenced the pinching behavior in the cyclic response [and so dissipated energy].
- The numerical model simulated the overall response of as-built specimens with an acceptable level. The crack patterns and cyclic response were consistent in the numerical and experimental results.
- After successful repair by the proposed method, the specimens that were heavily damaged recovered their former capacities. The crack pattern and failure mode of the repaired specimen indicated a non-axial failure mode after the tests on the repair. However, the bond-slip performance of the specimens was not significantly enhanced by the repair action.

## 5.2 Future Work

The retrofit of the RC columns before any pre-damage can provide a valuable contribution. As a retrofit material, a conventional CFRP material or other advanced materials like SMA will be implemented.

A suitable numerical modeling strategy for repaired specimens can be developed. The cyclic response under complex stress-strain mechanisms can be better revealed. The evaluation of internal stresses and damage can be investigated in depth by the reproduced response.

Owing to the more realistic assessment capability of the stochastic-based nonlinear FE analysis, which is now available in user-friendly computer tools, reproducing the structural response of substandard members by computational stochastic mechanics could yield more accurate results for assessment purposes. That should be implemented.

## REFERENCES

- ACI 318 (2019) Building code requirements for structural concrete and commentary (aci 318m-11), USA: American Concrete Institute
- ACI 408R-03 (2003) Bond and development of straight reinforcing bars in tension (aci-408r-03), USA: American Concrete Institute
- ACI 440.2R-17 (2017) Guide for the design and construction of externally bonded FRP systems for strengthening concrete structures, (aci-4440.2r-17), USA: American Concrete Institute
- AFAD (2012) Afet Raporu-Van Depremi, Disaster and Emergency Management Presidency, Ministry of Interior, Türkiye, Retrieved from: <https://www.afad.gov.tr/odenekler-harcamalar-kampanyalar>
- Angster S, Fielding EJ, Wesnousky S, et al (2015) Field reconnaissance after the 25 April 2015 M 7.8 Gorkha Earthquake. *Seismological Research Letters* 86:1506–1513. <https://doi.org/10.1785/0220150135>
- Arslan MH, Korkmaz HH (2007) What is to be learned from damage and failure of reinforced concrete structures during recent earthquakes in Turkey? *Engineering Failure Analysis* 14:1–22. <https://doi.org/10.1016/j.engfailanal.2006.01.003>
- ASCE SEI 41 (2017) Seismic evaluation and retrofit of existing buildings, American Society of Civil Engineers.
- ATENA Program Documentation, Part 1 (2014) Atena theory manual, Cervenka Consulting, <http://www.cervenka.cz/>
- Bal İE, Crowley H, Pinho R, Gülay FG (2008) Detailed assessment of structural characteristics of Turkish RC building stock for loss assessment models. *Soil Dynamics and Earthquake Engineering* 28:914–932. <https://doi.org/10.1016/j.soildyn.2007.10.005>
- Bazant Z, Oh B (1983) Crack band theory for fracture of concrete. *Materials and Structures* 16:155–177
- Bull D, Kam WY, Pampanin S (2009) Experimental validation of selective weakening approach for the seismic retrofit of exterior beam-column joints. In: New Zealand Society of Earthquake Engineering (NZSEE) Conference Christchurch, New Zealand
- Çağatay İH (2005) Experimental evaluation of buildings damaged in recent earthquakes in Turkey. *Engineering Failure Analysis* 12:440–452. <https://doi.org/10.1016/j.engfailanal.2004.02.007>
- Cardone D (2016) Fragility curves and loss functions for RC structural components with smooth rebars. *Earthquakes and Structures* 10:1181–1212. <https://doi.org/10.12989/EAS.2016.10.5.1181>

- CEN (2004a) Design of concrete structures - Part 1-1: General rules and rules for buildings. EN1992-1-1. Brussels, Belgium: Comité Européen de Normalisation (CEN)
- CEN (2004b) Design of structures for earthquake resistance - Part 1: General rules, seismic actions and rules for buildings. EN1998-1. Comité Européen de Normalisation (CEN), Brussels, Belgium
- CEN (2005) Design of structures for earthquake resistance - Part 3: Assessment and retrofitting of buildings. EN1998-3. Comité Européen de Normalisation (CEN), Brussels, Belgium.
- Cervenka V (1985) Constitutive model for cracked reinforced concrete. *ACI* 82:877–882
- Del Vecchio C, Di Ludovico M, Balsamo A, Prota A (2018) Seismic retrofit of real beam-column joints using fiber-reinforced cement composites. *Journal of Structural Engineering* 144:04018026. [https://doi.org/10.1061/\(ASCE\)ST.1943-541X.0001999](https://doi.org/10.1061/(ASCE)ST.1943-541X.0001999)
- Del Vecchio C, Eeri M, Di Ludovico M, Prota A (2020) Repair costs of RC building components: From actual data analysis to calibrated consequence functions. *Earthquake Spectra* 36:353–377. <https://doi.org/10.1177/8755293019878194>
- Del Zoppo M, Di Ludovico M, Balsamo A, Prota A (2018) Comparative analysis of existing RC columns jacketed with CFRP or FRCC. *Polymers* 10:361. <https://doi.org/10.3390/polym10040361>
- DEMP (2020) Preliminary report on Sivrice (Elazığ) earthquake with Mw of 6.8 (in Turkish), Ministry of Interior, Disaster and Emergency Management Presidency (DEMP), Turkey
- Di Pietro G, Mora T (2015) The effect of the L’Aquila earthquake on labour market outcomes. *Environ Plann C Gov Policy* 33:239–255. <https://doi.org/10.1068/c12121r>
- Duran B, Tunaboyu O, Avşar Ö (2017) Determination of elasticity modulus of low strength concrete and its effect on the risk assessment results by DSVB. *Journal of The Faculty of Engineering and Architecture of Gazi University* 32:253–264. <https://doi.org/10.17341/gazimmfd.300617>
- Dyngeland T (1989) Behavior of reinforced concrete panels. Dissertation, Trondheim University, BK-report 1989:1, Norway
- El-Amoury T, Ghobarah A (2002) Seismic rehabilitation of beam–column joint using GFRP sheets. *Engineering Structures* 24:1397–1407
- Eligehausen R, Popov E, Bertero V (1983) Local bond stress-slip relationship of deformed bars under generalized excitations, Report No. UCB/EERC-83/23, Earthquake Engineering Center, University of California, Berkeley.
- Elwood KJ (2006) Behavior and Modeling of Existing Reinforced Concrete Columns. EERI Presentation. In: 100th Anniversary Earthquake Conferenc Commemorating the 1906 San Francisco Earthquake. Available in: [http://www.1906eqconf.org/tutorials/SeisPerformExistConcrBldg\\_Elwood.pdf](http://www.1906eqconf.org/tutorials/SeisPerformExistConcrBldg_Elwood.pdf)

- Elwood KJ, Moehle JP (2003) Shake table tests and analytical studies on the gravity load collapse of reinforced concrete frames, Pacific Earthquake Engineering Research Center (PEER), College of Engineering, University of California: PEER report 2003/01.
- ESM 98 (1998) European Macroseismic Scale (EMS)
- FEMA 306 (1998) Evaluation of earthquake damaged concrete and masonry wall buildings: Basic procedures manual (FEMA 306), Federal Emergency Management Agency, USA
- FEMA 461 (2007) Interim protocols for determining seismic performance characteristics of structural and nonstructural components through laboratory testing (FEMA 461), Federal Emergency Management Agency, USA
- FEMA P58 (2018) Seismic performance assessment of buildings (FEMA P58), Federal Emergency Management Agency, USA
- fib (2010) Model code for concrete structures. Fédération Internationale du Béton (fib), Berlin: Ernst, Wilhelm & Sohn.
- fib Bulletin No. 25 (2003) Displacement-based seismic design of reinforced concrete buildings. State-of-art report. Fédération Internationale du Béton (fib). Lausanne, Switzerland.
- Gerges NN, Issa CA, Fawaz S (2015) Effect of construction joints on the splitting tensile strength of concrete. *Case Studies in Construction Materials* 3:83–91. <https://doi.org/10.1016/j.cscm.2015.07.001>
- Hassan WM, Elmorsy M (2022) Probabilistic beam–column joint model for seismic analysis of concrete frames. *J Struct Eng* 148:04022011. [https://doi.org/10.1061/\(ASCE\)ST.1943-541X.0003235](https://doi.org/10.1061/(ASCE)ST.1943-541X.0003235)
- HAZUS MR4 (2003) Multi-hazard loss estimation methodology. Earthquake Model (HAZUS MH. MR4), Technical Manual. Department of Homeland, Security, Emergency Preparedness and Response Directorate, FEMA
- Hordijk DA (1991) Local approach to fatigue of concrete. Ph.D. Thesis, Delft University of Technology, Netherlands
- JBDPA (2001) Guideline for post-earthquake damage evaluation and rehabilitation, Japan Building Disaster Prevention Association (JBDPA), Japan
- JRC (2007) Field manual for post-earthquake damage and safety assessment and short-term countermeasures (AeDES), Institute for the Protection and Security of the Citizen, Joint Research Centre (JRC), European Commission
- Kc A, Sharma K, Pokharel B (2019) Performance of heritage structures during the Nepal Earthquake of April 25, 2015. *Journal of Earthquake Engineering* 23:1346–1384. <https://doi.org/10.1080/13632469.2017.1360225>
- Kollegger J, Mehlhorn G (1988) Experimentelle und analytische untersuchungen zur aufstellung eines materialmodells für gerissene stahlbetonscheiben (in German), Nr.6 Forschungsbericht, Massivbau, Gesamthochschule Kassel

- Kolmar W (1986) Beschreibung der kraftübertragung über risse in nichtlinearen finite- element- berechnungen von stahlbetontragwerken (in German). Dissertation, T.H. Darmstadt
- Mander JB, Priestley MJN, Park R (1988) Theoretical stress-strain model for confined concrete. *Journal of Structural Engineering* 114:1804–1826. [https://doi.org/10.1061/\(ASCE\)0733-9445\(1988\)114:8\(1804\)](https://doi.org/10.1061/(ASCE)0733-9445(1988)114:8(1804))
- Masi A, Vona M (2009) Estimation of the in-situ concrete strength: provisions of the European and Italian seismic codes and possible improvements. Eurocode 8 Perspectives from the Italian Standpoint Workshop, Napoli, Italy, p 12
- Mazılıgüney L, Yaman İÖ, Azılı F (2008) In-situ concrete compressive strength of residential, public and military structures. In: 8th International Congress on Advances in Civil Engineering, Famagusta, North Cyprus
- Menegotto M, Pinto PE (1973) Method of analysis for cyclically loaded reinforced concrete plane frames including changes in geometry and non-elastic behaviour of elements under combined normal force and bending. In: International Association of Bridge and Structural Engineering (IABSE), Lisbon, Portugal. pp 15–22
- Menetrey Ph, Willam KJ (1995) Triaxial failure criterion for concrete and its generalization. *ACI, Structural Journal* 92:311–318. <https://doi.org/10.14359/1132>
- Mergos PE, Kappos AJ (2013) A combined local damage index for seismic assessment of existing RC structures: Damage index for seismic assessment of existing RC structures. *Earthquake Engng Struct Dyn* 42:833–852. <https://doi.org/10.1002/eqe.2247>
- MoEU (2020) Ministry of Environment and Urbanisation, Republic of Turkey, <https://csb.gov.tr/>
- Murcia-Delso J (2013) Bond-slip behavior and development of bridge column longitudinal reinforcing bars in enlarged pile shafts. Ph.D. Thesis, University of California
- Nakano Y, Maeda M, Kuramoto H, Murakami M (2004) Guideline for post-earthquake damage evaluation and rehabilitation of RC buildings in Japan. In: 13th World Conference on Earthquake Engineering, Vancouver, Canada
- Naseer A, Khan AN, Hussain Z, Ali Q (2010) Observed seismic behavior of buildings in northern Pakistan during the 2005 Kashmir earthquake. *Earthquake Spectra* 26:425–449. <https://doi.org/10.1193/1.3383119>
- Norton JA, King AB, Bull DK, et al (1994) Northridge earthquake reconnaissance report. *BNZSEE* 27:235–344. <https://doi.org/10.5459/bnzsee.27.4.235-344>
- NZS 3101 (2006) Standards New Zealand (SNZ), Concrete structures standard: part 1 – the design of concrete structures. NZS 3101:2006. Wellington: Standards New Zealand.
- Ozmen HB, Inel M, Senel SM, Kayhan AH (2015) Load carrying system characteristics of existing Turkish RC building stock. *International Journal of Civil Engineering* 13:16

- Öztürk M (2015) Field Reconnaissance of the October 23, 2011, Van, Turkey, Earthquake: Lessons from Structural Damages. *J Perform Constr Facil* 29:04014125. [https://doi.org/10.1061/\(ASCE\)CF.1943-5509.0000532](https://doi.org/10.1061/(ASCE)CF.1943-5509.0000532)
- Park R (1989) Evaluation of ductility of structures and structural assemblages from laboratory testing. *New Zealand Nat Soc Earthq Eng Bull* 22: 155–66.
- Park Y, Ang AH -S. (1985) Mechanistic seismic damage model for reinforced concrete. *Journal of Structural Engineering* 111:722–739. [https://doi.org/10.1061/\(ASCE\)0733-9445\(1985\)111:4\(722\)](https://doi.org/10.1061/(ASCE)0733-9445(1985)111:4(722))
- Parker M, Steenkamp D (2012) The economic impact of the Canterbury earthquakes. Reserve Bank of New Zealand: Bulletin 75:
- Priestley MJN, Calvi GM (1991) Toward a capacity-design assessment procedure for reinforced concrete frame. *Earthquake Spectra* 7:. <https://doi.org/10.1193/1.1585635>
- Randl N (2013) Design recommendations for interface shear transfer in *fib* Model Code 2010. *Structural Concrete* 14:230–241. <https://doi.org/10.1002/suco.201300003>
- Rankine W (1857) On the stability of loose earth. *Philosophical Transactions of the Royal Society of London* 147:.. <https://doi.org/10.1098/rstl.1857.0003>
- Ricci P, De Luca F, Verderame GM (2011) 6th April 2009 L'Aquila earthquake, Italy: reinforced concrete building performance. *Bull Earthquake Eng* 9:285–305. <https://doi.org/10.1007/s10518-010-9204-8>
- Shimizu Y, Hirosawa M, Zhou J (2000) Statistical analysis of concrete strength in existing reinforced concrete buildings in Japan. In: *Proceedings of the 12th World Conference on Earthquake Engineering (12 WCEE)*, Auckland, New Zeland, p 8
- TEC (1975) Turkish Earthquake Code, Specification for structures to be built in disaster areas. Turkey: Turkish Government Ministry of Reconstruction and Resettlement
- Tezcan SS, Yerlici V, Durguno HT (1978) A reconnaissance report for the Romanian earthquake of 4 March 1977. *Earthquake Engng Struct Dyn* 6:397–421. <https://doi.org/10.1002/eqe.4290060407>
- TRMCA (2020) Turkish Ready Mixed Concrete Association, Elazığ earthquake reconnaissance report (in Turkish), <http://www.thbb.org/teknik-bilgiler/raporlar/elazig-depremi/>, Retrieved 01 March 2020
- Van Mier JGM (1986) Multiaxial strain-softening of concrete, Part I: Fracture. *Materials and Structures, RILEM* 19:
- Vecchio FJ, Collins MP (1986) Modified compression-field theory for reinforced concrete beams subjected to shear. *ACI Journal* 83:219–231
- Verderame GM, De Carlo G, Ricci P, Fabbrocino G (2009) Cyclic bond behaviour of plain bars. Part II: Analytical investigation. *Construction and Building Materials* 23:3512–3522. <https://doi.org/10.1016/j.conbuildmat.2009.07.001>

- Yılmaz N, Avşar Ö (2013) Structural damages of the May 19, 2011, Kütahya–Simav earthquake in Turkey. *Natural Hazards* 69:981–1001. <https://doi.org/10.1007/s11069-013-0747-2>
- Yurdakul Ö, Artagan SS, Balaban E, Rouil L (2022) Evaluation of cyclic bond-slip behavior of smooth bars in low strength concrete: An experimental and stochastic study. *Structures* 41:568–585. <https://doi.org/10.1016/j.istruc.2022.05.036>
- Yurdakul Ö, Duran B, Tunaboyu O, Avşar Ö (2021) Field reconnaissance on seismic performance of RC buildings after the January 24, 2020 Elazığ-Sivrice earthquake. *Nat Hazards* 105:859–887. <https://doi.org/10.1007/s11069-020-04340-x>